DEPOSITIONAL ENVIRONMENTS AND PROVENANCE OF THE DEL RIO FORMATION IN WEST TEXAS

A Thesis

by

WILLIAM WALKER LIGON

Submitted to the Office of Graduate and Professional Studies of
Texas A&M University
in partial fulfillment of the requirements for the degree of

MASTER OF SCIENCE

Chair of Committee,	Michael C. Pope
Committee Members,	Brent Miller
	Walter Ayers
Head of Department,	Michael C. Pope

August 2017

Major Subject: Geology

Copyright 2017 William Walker Ligon

ABSTRACT

The Middle Cretaceous Del Rio Formation is a calcareous shale interbedded with a few thin sandstone and limestone beds. The extreme variability within this unit makes it difficult to correlate regionally. However, analyzing outcrop data, hand samples, thin sections, core descriptions, wire line logs, and detrital zircons provides a clearer understanding of the regional stratigraphy, thickness variations, provenance and depositional environments of the Del Rio Formation across the Maverick Basin and west Texas.

The various lithologies within the west Texas Del Rio Formation are grouped into six facies that indicate deposition occurred in a shallow, subtidal marine environment within storm wave base. The facies and sedimentary structures indicate the Del Rio Formation was deposited on a homiclinal ramp. A ramp model is supported by the abundance of preserved storm deposits, and variability of facies and bedding among the outcrop sections. Sequences within the Del Rio Formation are inferred to be autocyclic because of the apparent randomness of facies distributions, and unresolvable sequence stratigraphic patterns within the measured sections. However, the Del Rio Formation as a whole is interpreted to be a single sequence representative of a lowstand preceding the Late Cenomanian transgression that deposited the Buda, Eagle Ford, and Austin Chalk formations.

The variability of thickness of the Del Rio Formation is due to onlap against pre-existing topography of the Lower Cretaceous Edwards platform, and erosion beneath the

Buda. The pre-existing Terrell and San Marcos Arches not only affected the thickness of the unit, but also the regional depositional settings. The Paleozoic Terrell Arch substantially impeded sediment transport to the west and therefore the depositional environment that produced the sandstone and siltstone beds to the east did not reach west of the arch.

The detrital zircon spectrum within the Del Rio formation contains age peaks corresponding to the Late Mesoproterozoic to Early Neoproterozoic (900-1300 Ma), Neoproterozoic/ Cambrian (500-650 Ma), Middle Paleozoic (350-500 Ma), Jurassic (170-175 Ma), and Middle Cretaceous (99-100 Ma).The siliciclastic grains within the Del Rio Formation were derived from multiple provenances. The most viable sources include the Ouachita Orogeny (recycled Gondwanan and Appalachian sediments), the Llano Uplift, and western volcanic arcs during the Jurassic and the Sevier Orogeny.

CONTRIBUTORS AND FUNDING SOURCES

Contributors

This work was supported by a thesis committee consisting of Dr. Michael C. Pope (advisor), Dr. Brent Miller of the Department of Geology, and Dr. Walt Ayers of the Department of Petroleum Engineering.

The field work for this study was aided by the help of field assistants Adam Mattson and Kyle Gillespie. Crushing of rock samples and hand sample analysis was aided by the help of lab assistants Cameron Ramsey, Zach Bordovksy, and Matthew Hyde. Detrital zircon geochronology was done at the Department of Geology and Geophysics at the University of Houston under the supervision of Dr. Tom Lapen. The core study was done at the Bureau of Economic Geology in Austin, TX.

All other work conducted for the thesis was completed by the student independently.

Funding Sources

Graduate study was supported by a Teaching assistantship from Texas A&M University as well as a grant provided by the Geological Society of America.

TABLE OF CONTENTS

Page

ABSTRACT……..……...…….. ii

CONTRIBUTORS AND FUNDING SOURCES……....……. iv

TABLE OF CONTENTS……...……..…….. v

LIST OF FIGURES……...……..……...…… vii

LIST OF TABLES……....……...…. ix

1. INTRODUCTION……...……..…….. 1

2. GEOLOGICAL BACKGROUND……....…….……. 5

3. METHODS…….……....……..……. 11

    3.1 Outcrop……..……..…….…… 11
    3.2 Subsurface……..……..…….…... 12
    3.3 Provenance……..……...……. 13

4. RESULTS…….…….…… 18

    4.1 Facies Analysis……..…..……...…….…… 18
    4.2 Core Analysis……..……..……....……... 22
    4.3 Thickness Trends……..…….……. 24
    4.4 Detrital Zircon Results……. 26

5. DISCUSSION…….……...…….…….. 29

    5.1 Depositional Setting….……..……. 29
    5.2 Thickness Variations..……..……..…… 34
    5.3 Provenance…….……..…… 37
        5.3.1 Mesoproterozoic/ Early Neoproterozoic (900-1300 Ma).... 37
        5.3.2 Neoproterozoic/ Cambrian (500-650 Ma)…...…...…….… 38
        5.3.3 Middle Paleozoic (350-500 Ma)……..…...…….…….. 40
        5.3.4 Jurassic (170-175 Ma)……...……...…….. 41
        5.3.5 Middle Cretaceous (99-100 Ma).…….…….. 41

Page

5.3.6 Provenance Discussion……...……. 42

6. CONCLUSIONS…..…….…… 48

REFERENCES…….……... 50

APPENDIX A…….…… 57

APPENDIX B…….……...……. 68

APPENDIX C……. 69

LIST OF FIGURES

		Page
Figure 1	Modified Blakey map displaying study area 100 Ma…….	2
Figure 2	Map of study area with outcrop locations, core location, and potential sources of siliciclastics for the region…..…...	4
Figure 3	Stratigraphic column of Cretaceous strata in west Texas.....	7
Figure 4	Full section of the Del Rio Formation at the Seminole Canyon Outcrop……..…..……	7
Figure 5	Sedimentary structures field photos……..…..…….	9
Figure 6	Paleobiology field photos……...…….	10
Figure 7	Zircon maps of samples WC2b and EC1b…...……	15
Figure 8	Cross section of measured outcrops across west Texas……	20
Figure 9	East Pecos River measured section displaying random distribution of facies within the Del Rio Formation……..……...	21
Figure 10	Measured section of Boring ID 12 core including photos of identified facies……..…….	23
Figure 11	Map of Del Rio Formation outcrops displaying measured thickness……..……	25
Figure 12	Reference map and isopach of the Del Rio Formation in the Maverick Basin, west Texas……..……	25
Figure 13	Cross section of outcrops and well logs……..……	26
Figure 14	Relative probability plot, samples WC2b and EC1b, Del Rio Formation near Pecos River, west Texas…..…….	28
Figure 15	Ramp profile diagram……...……...	30

Page

Figure 16	Probability density plots of the Del Rio Formation samples, and other formations derived from the Appalachian or Ouachita Orogenies…….	45
Figure 17	Probability density plots for Del Rio Samples EC1b and WC2b with interpreted provenance……..	46
Figure 18	Modified Blakey map of North America (100 Ma), displaying the direction of sedimentation of viable sediment sources……	47

LIST OF TABLES

Page

Table 1 Table of interpreted facies with diagnostic characteristics…… 19

1. INTRODUCTION

During the Middle to Late Cretaceous, shallow marine carbonate deposition of the interior North American plate was dominated by the Western Interior Seaway (WIS). During the Cenomanian, the developing WIS created shallow marine environments for the interior North American craton and modern-day west Texas (Fig. 1). The Del Rio Formation is an interbedded calcareous shale, skeletal limestone and rare sandstone beds that outcrops in west Texas and extends laterally throughout the subsurface dipping gently towards the Gulf Coast. Previous research on the Del Rio Formation focused on understanding the depositional environment of the unit through fossil identification and interpretation of sedimentary structures (Lock, 2007 and 2009; Mancini, 1979). This study utilizes outcrop data, including hand-held gamma ray profiles, hand sample analysis, and thin section analysis, core descriptions, log analysis, and detrital zircon geochronology to understand the regional stratigraphy, thickness variations, provenance and depositional environments of the Del Rio Formation across the Maverick Basin and west Texas.

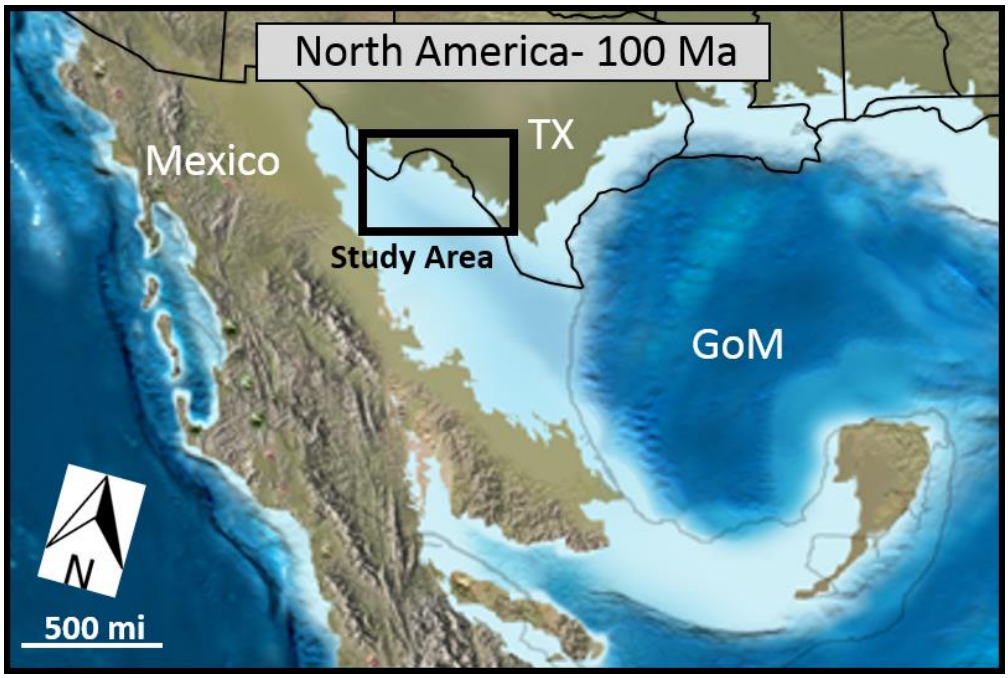

Figure 1. Modified Blakey map displaying study area 100 Ma. (Blakey et al., 1988)

The source of siliciclastic grains within the shale and carbonate dominated Del Rio Formation has not been determined. The siliciclastic units are interpreted to be shallow-water storm deposits on the basis of hummocky cross-stratification (Lock, 2008). Sources for the siliciclastic grains were speculated to be the Diablo Platform or the Llano Uplift (Lock, 2009), but no geochronological studies have been done to support these theories. Precambrian/ Upper Paleozoic units of the Llano Uplift, as well as the Ouachita Mountains and Marathon Uplift were considered potential source areas for siliciclastic grains in Middle Cretaceous strata of west Texas (Phelps et al., 2014). In this project, detrital zircons were analyzed using Laser Ablation Inductively Coupled Plasma Mass Spectrometry (LA-ICP-MS) to determine whether the provenance of the

coarser siliciclastic sediments was local (e.g. Llano Uplift, Marathon Uplift) or more distal (e.g. Ouachitas). Detrital zircons are ubiquitous in sandstones due to their highly resistive nature to both chemical and physical weathering (Thomas, 2011). The age of a single zircon grain is interpreted to be the crystallization age of the source rock. LA-ICP-MS is a U-Pb dating method that uses microbeam analyses to determine zircon ages with reasonable accuracy (Mattinson, 2013; Chang et al., 2006). Understanding the source of the siliciclastic sediments will provide constraints on the sediment transport of the Del Rio Formation. This prominent shale and carbonate unit likely records a long-term sea level lowstand following deposition of the carbonate-rich Edwards Group/Georgetown Formation sediments.

The study area includes multiple counties in west Texas (Fig. 2). The outcrops studied are located west of Del Rio, TX, along Texas Highway 90, in Big Bend National Park, and near the town of Terlingua (Val Verde, Terrell, and Brewster counties). Well log analysis was focused in the Maverick Basin (Dimmit, Zavala, and Maverick counties). The cores analyzed during this study are from Val Verde County, located between the outcrops and the Maverick Basin. They were used to correlate measured sections with subsurface sections (Fig. 2).

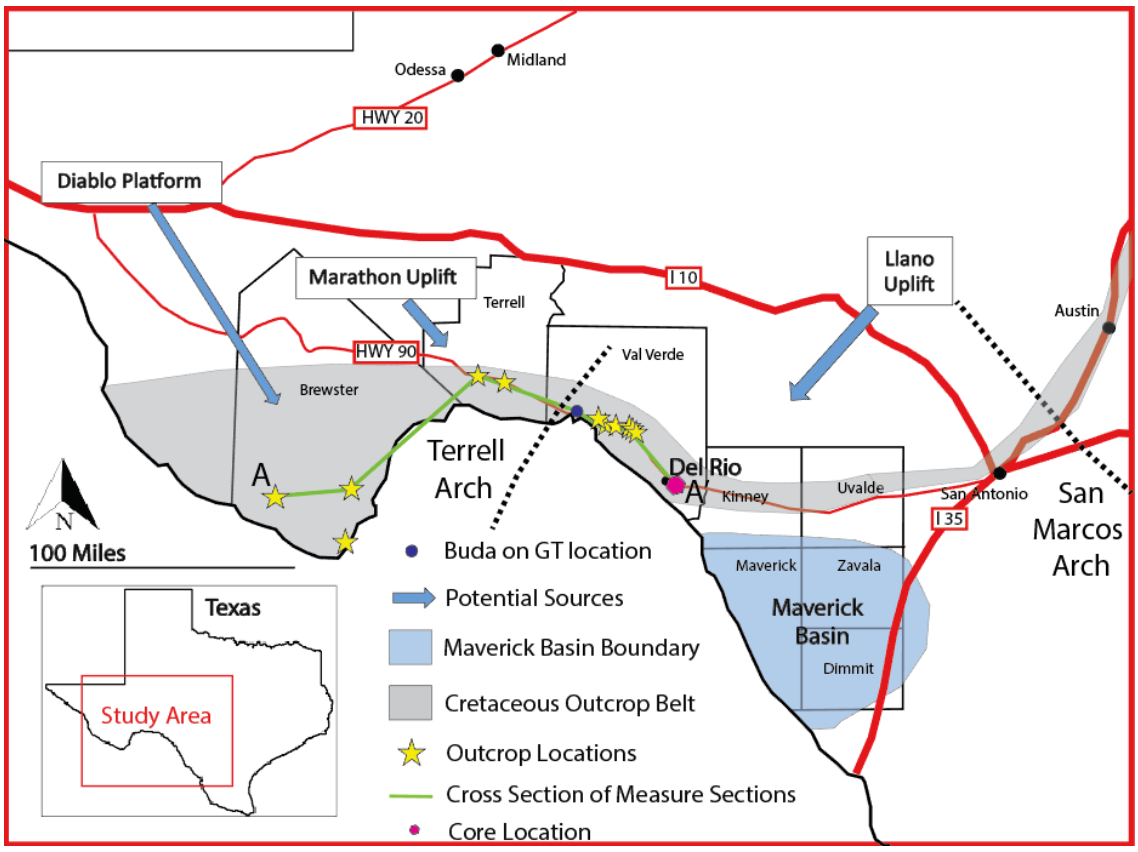

Figure 2. Map of study area with outcrop locations, core location, and potential sources of siliciclastics for the region.

2. GEOLOGIC BACKGROUND

Cretaceous strata record extremely warm climate conditions dominated by very high sea levels and development of shallow epicontinental seas (Dean and Arthur, 1998). A unique set of tectonic, climatic and oceanographic conditions during the Cretaceous promoted the development of abundant carbonate platforms (Phelps et al., 2014). The warm climatic conditions are hypothesized to be the result of global greenhouse conditions around 100 Ma that were caused by a rise in atmospheric carbon dioxide due to increased volcanic activity (Leckie et al., 1998).

The Cretaceous is characterized by numerous "Oceanic Anoxic Events" (OAEs) that coincided with increased volcanic activity (Phelps et al., 2014). These events represent time intervals of oxygen deficient oceans coupled with the burial of organic carbon in marine sequences (Schlanger and Jenkyns 1976; Phelps et al., 2014). OAEs often ceased carbonate sediment production and initiated the deposition of anoxic shale intervals on carbonate platforms (Weissert et al., 1998). The Cenomanian in west Texas records shelf drowning following an oceanic anoxic event documented by the termination of shallow-water carbonate deposition and accumulation of anoxic shale and chalk deposits on a distally steepened ramp (Phelps et al., 2014). The Cenomanian Del Rio Formation records of the deposition of a calcareous shale with numerous limestone and rare sandstone beds over a carbonate platform after complete drowning of the Albian Edwards Group reef margin.

By the Middle Cretaceous deposition of the Edwards Group produced high relief

carbonate margins (Fisher and Rodda, 1969). During a subsequent transgressive event the Georgetown Formation was deposited filling or partially filling the pre-existing topography (Rose, 1974). The Early Cenomanian Del Rio Formation was deposited unconformably on the Georgetown Formation and it, in turn, is unconformably overlain by Buda Limestone (Fig. 3). The Del Rio Formation is a mixed siliciclastic-carbonate unit consisting of interbedded calcareous shale, calcareous sandstone, and skeletal packstone. The Del Rio Formation crops out in west Texas, west of the San Marcos Arch, and is a relatively thick shale unit between the underlying carbonate-rich Edwards/ Georgetown Group and the overlying carbonate-rich Buda, Eagle Ford and Austin Chalk (Fig. 4). Thin interbeds of limestone and siliciclastic sandstone occur throughout the Del Rio Formation section in west Texas, but commonly, they are laterally discontinuous and difficult to correlate regionally (Lock, 2013). The onlapping nature of this unit, the absence of continuous marker beds and the variable amount of erosion along the upper surface of the Del Rio Formation makes correlation among outcrops problematic (Lock, 2008). The Del Rio Formation shows extreme regional thickness variations throughout west Texas, being 6-82 m thick over short distances (Lock et al., 2007; Maxwell and Dietrich, 1972). Thickness fluctuations of the unit may be the result of depositional onlap onto substantially irregular paleotopography of the underlying Edwards/ Georgetown Group carbonate platform, combined with erosion at the Buda/ Del Rio Formation unconformity (Lock, 2013; Donovan et al., 2012).

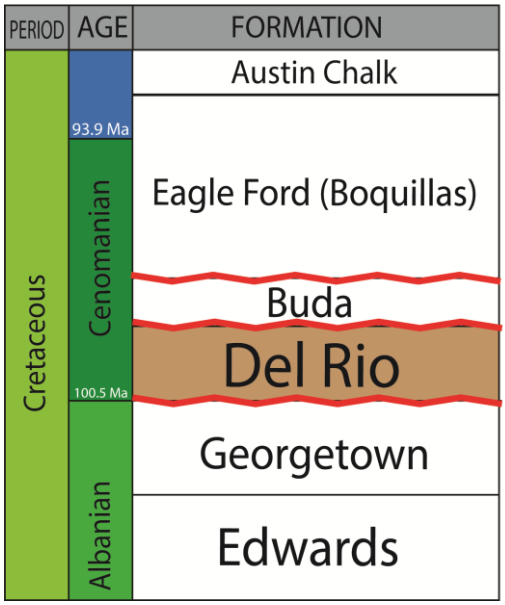

Figure 3. Stratigraphic column of Cretaceous strata in west Texas. Ages from Ogg and Hinnov, 2012**.**

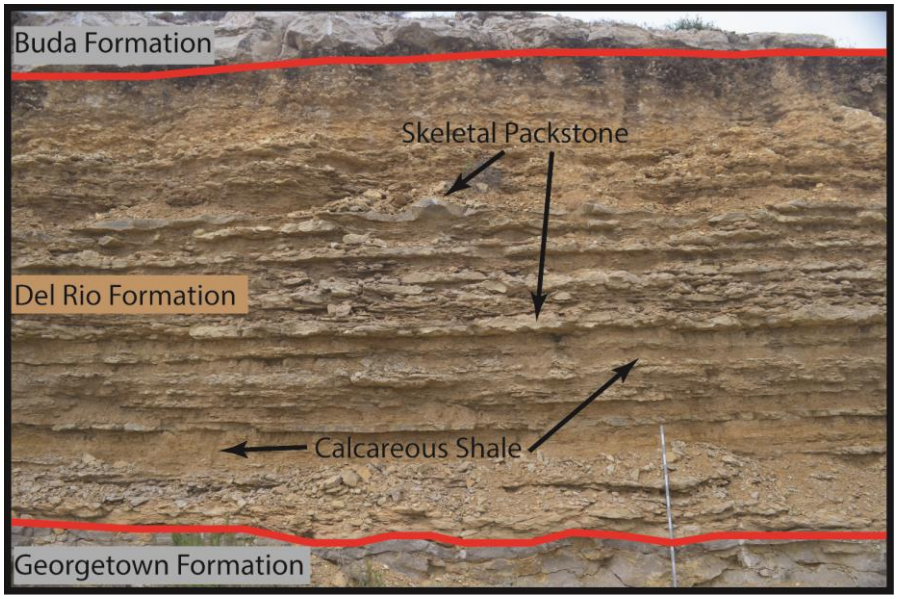

Figure 4. Full section of the Del Rio Formation at the Seminole Canyon Outcrop. 1.6 meter Jacob's staff for scale. The red lines mark the unconformities between the Georgetown Formation and the Del Rio Formation (lower), and the Del Rio and Buda Formations (upper). Note the thin beds of skeletal packstone and calcareous shale.

The directions and sources of sediment transport for the Del Rio Formation are unknown. Previous research suggests that sediment accumulation in west Texas during the Middle Cretaceous was locally controlled by the structural features of the Maverick Basin, and Central Texas and San Marcos Platforms, and Stuart City Reef trend. Carbonate deposition was influenced by an influx of siliciclastic sediments from the northeast during an early Cenomanian marine transgressive phase (Mancini, 1974). Previous hypotheses suggested the Llano Uplift and Marathon Uplift were local terrigenous sources, and the Ouachita Mountains were a more distal source during the Cenomanian (Lock, 2009; Phelps et al., 2014). Another potential source of siliciclastic sediments is the Precambrian rocks of the western Diablo Platform.

Though the section is dominated by calcareous shale, laminated lime siltstone facies also occur and contain abundant hummocky cross stratification. Sandstone beds are rare and are characterized by very fine, sub-rounded grains, usually dominated by quartz but also containing calcite cement and glauconite. The various lithologies, sedimentary structures, and macrofossil evidence within the Del Rio Formation indicate a shallow marine depositional environment susceptible to episodic storms (Lock, 2008; Lock, 2013). During the Cretaceous, west Texas was at latitude 15°N, within the zone of tropical hurricanes (Lock et al., 2009). The occurrence of HCS and tempestite bedding as well as starved ripples within the skeletal limestone beds implies high-energy storm deposition in a shallow water marine environment (Yang, 2005; Holland, 1997). HCS (Fig. 5) are formed in shallow marine environments at a depth of water below fair

weather wave base and above storm-weather wave base, likely within a few 10's of meters (Mauldin, 1985; Lock, 2013).

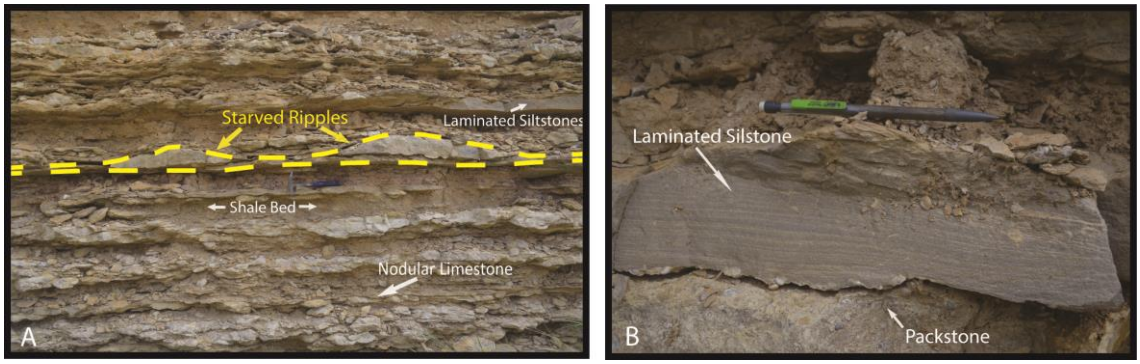

Figure 5. Sedimentary structure field photos. A) East Pecos River outcrop displaying interbeds and starved ripple sedimentary structures, hammer for scale. B) East Pecos River outcrop photo of a tempestite bed displaying HCS, pencil for scale.

The principal faunal elements (Fig. 6A) of the Del Rio Formation are oysters (*Ilymatogyraarieta*) and arenaceous forams (*Cribratina texana*), which indicate a brackish water influence (Lock, 2009; Mancini, 1979). Other fossils (Fig. 6B) include ammonites (*Mariella brazoensis*), gastropods, echinoids, and brachiopods. Horizontal tubular burrow trace fossils (*Ophiomorpha, Thalassinoides, and Spongeliomorpha*) occur at the base of the lime mudstone (Fig. 6C) and tempestite beds (Lock, 2009). Nodular bedding within the limestone units was caused by bioturbation and differential cementation and compaction during early burial (Mullins et al., 1980).

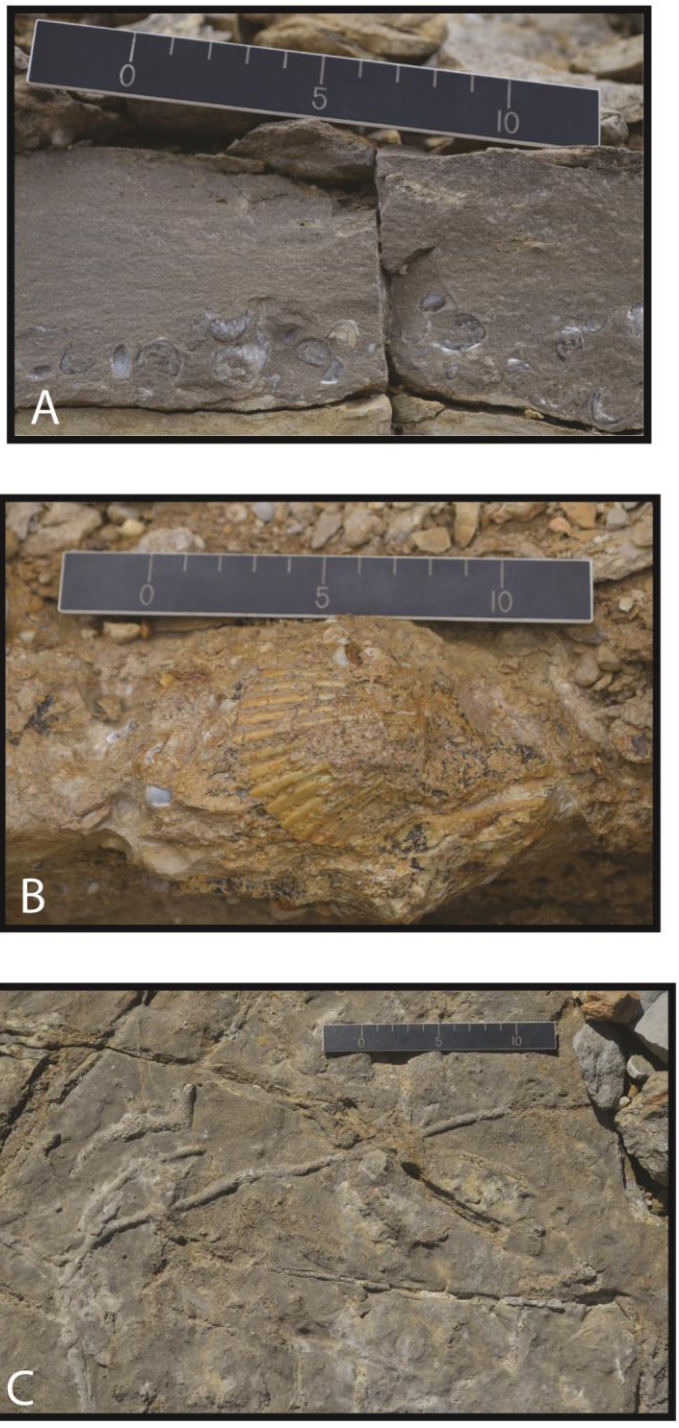

Figure 6. Paleobiology field photos. A) East Comstock outcrop photo of oyster species (*Ilymatogyraarieta*). B) Brachiopod at the East Comstock Outcrop. C) Burrow Trace Fossils (*Thalassinoides*) at Dagger Flats outcrop.

3. METHODS

3.1 Outcrops

To determine the geologic history of the Del Rio Formation, in west Texas, 11 outcrops of this unit north and west of the Maverick Basin (Fig. 2), were described bed-by-bed, and a hand-held gamma ray log was constructed for each outcrop. Hand samples from outcrops were described, and their thin sections were analyzed petrographically. Subsurface cores were described bed-by-bed, well logs were analyzed and correlated, and detrital zircon geochronology from outcrop samples was used to determine provenance of coarse siliciclastic sediments. The sections were measured using a 1.6 m Jacob's staff, then, stratigraphic columns of the outcrop sections were generated using Adobe Illustrator, incorporating lithology, sedimentary structures, fossil assemblages, facies variations, and contact descriptions with the bounding units. Hand-held gamma ray profiles were generated for each measured section using a Radiations Solutions MS-230 scintollimeter in order to correlate the surface exposures with subsurface wireline logs and core descriptions. The gamma ray profiles were collected with a 0.4 m sampling increment. The hand held scintollimeter recorded the percent of Potassium (K), Uranium (U), and Thorium (Th) in the rock. Equation 1 calculates the natural radiation of the unit (API) which were then plotted in order to create a gamma ray signature for each measured outcrop. Tying the exposed section of the Del Rio Formation with subsurface sections in well logs across the Maverick Basin aided in understanding regional thickness and stratigraphic variations of this unit.

*Eq. 1: API = (K*15) + (U*8) + (Th*4)*

Hand samples of representative Del Rio Formation facies were used for petrographic, geochemical, and stable isotope analysis. Hand samples were cut and polished to observe the mineralogy and sedimentary structures of the Del Rio Formation facies. The samples were polished using 320, 600, and 1000 μm grade silicon carbide abrasive grit. Thin sections were made from the hand samples collected in the field to further determine lithology and fossil assemblages.

3.2 Subsurface

Wireline logs and cores of the Del Rio Formation across the Maverick Basin were used to determine the regional thickness variations of this unit in the study area. From Drillinginfo's database, 96 well logs within Dimmit, Zavala, and Maverick counties were correlated across the Maverick Basin. After establishing a type log based on Hentz and Ruppel (2011), Techlog was used to regionally correlate the Del Rio Formation gamma ray and resistivity logs. The carbonate-rich Buda Formation's blocky low gamma ray signature was used as a marker bed to identify the underlying Del Rio Formation. The Del Rio Formation is characterized by high gamma ray values and low resistivity values. Once formation boundaries were picked in all well logs, the thicknesses were used to generate an isopach map of the Del Rio Formation across the Maverick Basin using ArcGIS. The thickness variations on this map were used to assess the effect of paleotopography during deposition.

Additionally, two water-well cores (Boring ID 12; Laughlin AFB) from Val Verde County, TX, containing the Del Rio Formation were measured and described bed-by-bed. These cores were available at the Bureau of Economic Geology in Austin, TX. Stratigraphic columns of the core sections were generated using Adobe Illustrator, incorporating lithology, sedimentary structures, fossil assemblages, facies variations, and contact descriptions with the bounding units (Appendix B). The cores in this study did not have available wireline logs, so a wireline log from another water well drilled nearby from the same company in Kinney County, TX was used for correlation between outcrops, core, and wireline logs within the basin. The gamma ray profiles from the outcrops north of the Maverick Basin were correlated to the core section and also into wireline logs across this basin to strengthen the regional subsurface interpretations.

3.3 Provenance

Detrital zircon geochronology was used to determine the provenance of coarser siliciclastic grains within the Del Rio Formation. Zircons were separated from the sandstone samples, one from the East Comstock outcrop and the other from the West Comstock outcrop. Mineral separation was completed at Texas A&M University's Department of Geology & Geophysics facilities. Detrital zircons were extracted from their host rock using conventional separation techniques. Each sandstone sample was crushed using a Bico Jaw Crusher and then pulverized using a Bico Disc Mill. The processed samples were then sieved using a Fisher Scientific Company U.S.A. standard testing sieve to obtain grains between 63-300 μm. The elutriated grains were then

separated using a Wilfley Table. Afterwards, the lighter minerals were discarded and the heavy minerals were chemically separated using Methylene Iodide (MEI) heavy liquids separation (ρ=3.32 g/cm^3), which separates greater density minerals (zircon: 4.6-4.8 g/cm^3) from the sample. Zircons and additional minerals that fall out of suspension in MEI were transferred to a petri dish and examined under a binocular microscope. Using a dental pick, the individual zircon grains were physically separated from the other accessory minerals using an Olympus SZ61 Zoom Stereo microscope. Details on the morphology and optical properties of zircon are available in Corfu et al. (2003) and Fedo (2003).

Once isolated, detrital zircons were mounted onto a strip of double-sided adhesive tape attached to a 0.5 x 2 cm glass plate. Each glass plate contained a minimum of 300 detrital zircon grains and was labeled corresponding to the outcrop source. Using a Zeiss microscope provided by Dr. Nicholas Perez at Texas A&M University, the two glass plates were imaged in order to create a zircon map to keep track of which zircons were analyzed (Fig. 7). Each plate was then placed on a puck along with two zircon standards provided by the University of Houston. The primary zircon standard (337.13 ± 0.37 Ma) used was a Plešovice zircon originating from granulite in the southern Bohemian Massif, Czech Republic (PLEIS) (Slama et al., 2008). The secondary zircon standard (1099.1 ± 0.5 Ma) was FC5Z from the Duluth Complex in Minnesota, USA (Heinselman, 1996; Jirsa et al., 2006). The purpose of the primary zircon standards were to calculate fractionation factors, which are applied to the detrital zircon sample. Fractionation factors are determined by dividing the known isotopic ratios of primary

zircon standards by the average value of all non-erroneous calculated data of that respective standard on a given day. Secondary zircon standards were used to determine the relative reproducibility and precision of detrital zircon sample data. Since the ages of secondary zircon standards are known, comparing fractionation factor corrected ages with the known age of secondary standards gives an indication of the reliability of analyzed detrital zircon sample data.

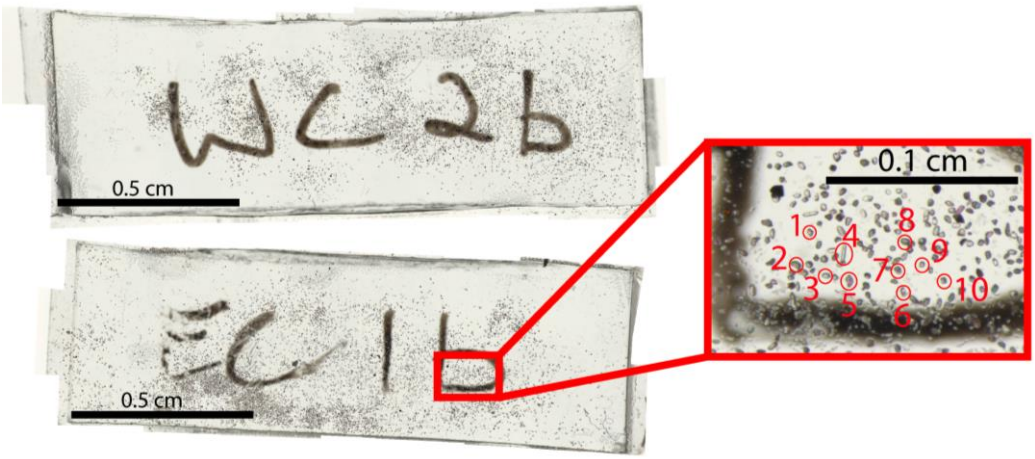

Figure 7. Zircon maps of samples WC2b and EC1b

Once the two zircon samples and zircon standards were placed on a puck, laser ablation inductively coupled plasma mass spectrometry (LA-ICP-MS) was used in the ICP Analytical Laboratory & Agilent Facility Center at the University of Houston to acquire the crystallization age of each zircon. This analysis was done under the supervision of Dr.

Thomas Lapen and his graduate students at the University of Houston. The laser ablation system was powered by an ATLex 300si laser and operated with a fluence of 2.99 J/cm^2 and grain ablation laser repetition rate of 8 Hz. Using a 20 μm spot size for the laser diameter, 150 grains were ablated for sample EC1b, and 140 grains were ablated for sample WC2b. The order of grain ablation and data collection for each sample began 4 samples of the primary standard, PLEIS, and 1 sample of the secondary standard, FC5Z, in order to calibrate the laser. Data analysis for each sample was conducted in the following order: analysis of one primary zircon standard (PLEIS 1), one secondary zircon standard (FC5Z 1), 10 grains (from sample "X"), one primary zircon standards (PLEIS 2), ten additional grains (sample "X"). This order of 23 analyses was termed one group. Grouping of grains was repeated until 120 sample grains were analyzed for each sample. Data acquisition for one grain lasts approximately 60 seconds and is termed a sequence. This includes approximately 15 seconds of brief laser warm-up and background measurement time, then approximately 35 seconds of grain ablation, and then 10 seconds of wash out time. The sequence is repeated after the laser spot is repositioned above the next selected grain.

After laser ablation was complete, the data was exported to an Excel file and imported into data reduction software provided by the University of Houston to filter useful and unusable data. This program filtered the reduced data of the raw isotopic measurements and automatically plotted fractionation corrections for user-defined standard isotopic ratios. The final ages, isotopic ratios, and associated 1σ absolute error values were selected from Pb^{206}/U^{238} or Pb^{207}/Pb^{206} values based on an 800 Ma cutoff

age. Pb^{206}/U^{238} values were used if ages were less than 800 Ma because Pb^{207}/Pb^{206} ages are more affected by lead loss in younger rocks. Obtaining ~100 or more useable analyses is a common goal for detrital zircon analyses, this number varies between studies and depends on the analysis method (e.g., Lawton et al., 2009; Craddock and Kylander-Clark, 2013, Mackey et al., 2012). For this study, usefulness of data and useable analyses refers to U-Pb isotopic data for a respective grain that are less than 20% discordant. The number of useable analyses obtained for WC2b and EC1b samples was 101 and 117 respectively.

The concordant zircon ages for each sample were then plotted in Excel in order to create probability density plots of the final detrital zircon ages. Isoplot 4.14 was used to generate probability density plots for each sample. These histograms were used to interpret the provenance of the Del Rio Formation by matching the ages for each sample's zircon grains with potential source areas.

4. RESULTS

4.1 Facies Analysis

Based on field observations, sedimentary structures, and hand sample and thin section analysis, six facies were identified within the Del Rio Formation. These facies are: 1) nodular lime mudstone, 2) shallow marine sandstone, 3) shallow marine siltstone, 4) interbedded skeletal packstone, grainstone and calcareous shale, 5) interbedded skeletal wackestone and calcareous shale, 6) and calcareous shale. See Table 1 for more detail.

Measured sections were generated for each outcrop (Appendix A) incorporating lithology, facies distribution, gamma ray profile, and fossil asssemblage. A cross-section with the most complete sections of the Del Rio Formation within the study area was generated to display the facies distribution across west Texas (Fig. 8). The Del Rio Formation thickens to the east and west across the study area and on either side of the Terrel Arch where the Del Rio Formation is not present. Thickness of the Del Rio Formation varies from 0 m on top of the Terrell Arch, to 37 m flanking the arch. East of the Terrell Arch, the Del Rio Formation contains more siliciclastic beds (sandstone and siltstone) as well as fossiliferous limestone (skeletal wackestone and packstone). West of the Arch, the section is dominated by shale and nodular limestone. The east Pecos River outcrop (Fig. 9) was designated an informal type section to further analyze the parasequences within the Del Rio Formation. Cyclicity within the east Pecos River outcrop appears to be random, and no pattern of facies seems to be repeated. However,

Facies	Lithology	Sedimentary Structures/ Description	Fossils	Bioturbation Index	Average Bed Thickness	Interpretation
A	Nodular Lime Mudstone	Limestone nodules, abundant burrows, massive	Oysters (*Ilymatogyra arietina*), benthic forams	5	0.1-0.3 m	Shallow water
B	Very Fine Sandstone	Very fine grained, well-sorted, sub-rounded/ rounded sand grains, poorly cemented, horizontal laminations common, predominately quartz	None	2	0.2 m	Shallow Marine Sandstone
C	Silty Limestone	Siliciclastic silt grains (50%), well-sorted, Hummocky Cross-Stratification (HCS), burrows, horizontal bedding, well consolidated, calcareous mud matrix	None	2	0.05-0.3 m	Shallow Marine Siltstone storm deposit
D	Skeletal Packstone and Grainstone	Mega-ripples, hummocks (lens-like), poorly sorted, skeletal grains or fragments, calcareous mud matrix	Oysters (*Ilymatogyra arietina, Exogyra cartledgei*), arenaceous forams (*Cribatina texana*), ammonites, clams, brachiopods, bivalves, planktonic forams, benthic forams	2	0.05-0.5 m	Mid ramp, shallow marine storm
E	Skeletal Wackestone	Poorly-sorted, skeletal grains, calcareous mud matrix	Oysters (*Ilymatogyra arietina*), arenaceous forams (*Cribatina texana*), brachiopods, shell fragments, planktonic forams, benthic forams	2	0.1- 0.2 m	Mid ramp, shallow marine storm
F	Calcareous Shale	Horizontal laminations, friable, fissile, indurated, easily weathered, burrows	Oysters (*Ilymatogyra arietina*), ammonites (*Mariella brazoenis*), benthic forams, planktonic forams, ostracods, echinoids	2-5	Variable range from 0.1-3 m	Lower ramp, shale deposit

Table 1. Table of interpreted facies with diagnostic characteristics. Bioturbation based off a 1-5 index, very low to very high bioturbation, respectively (Droser and Bottjer, 1986). For specifics on species of forams refer to (Mancini, 1974; Mauldin, 1985)

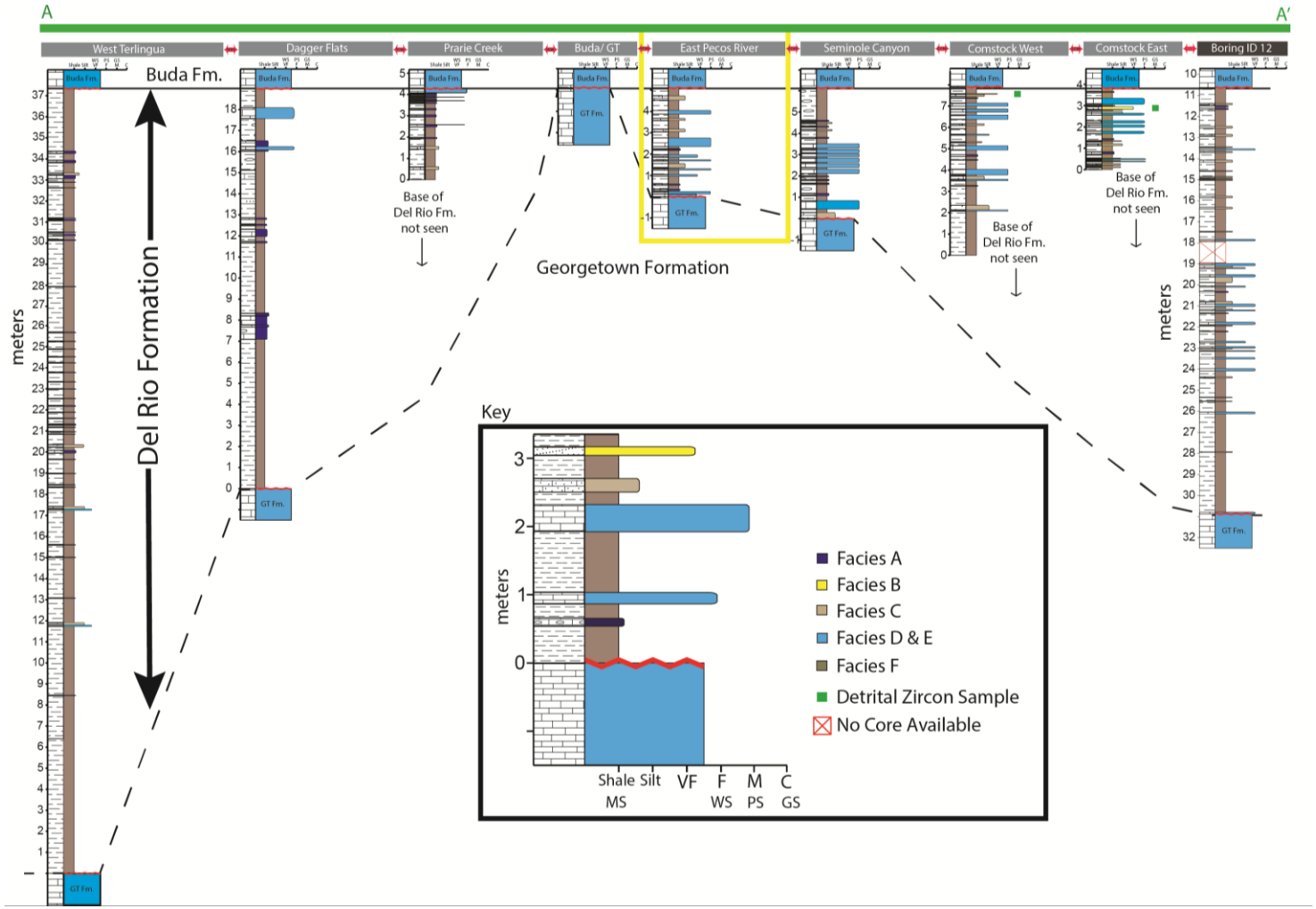

Figure 8. Cross section of measured outcrops across west Texas (Fig. 2). Colors in measured sections correspond with facies table (Table 1). Boring ID 12 is representative of the core section from Val Verde County.

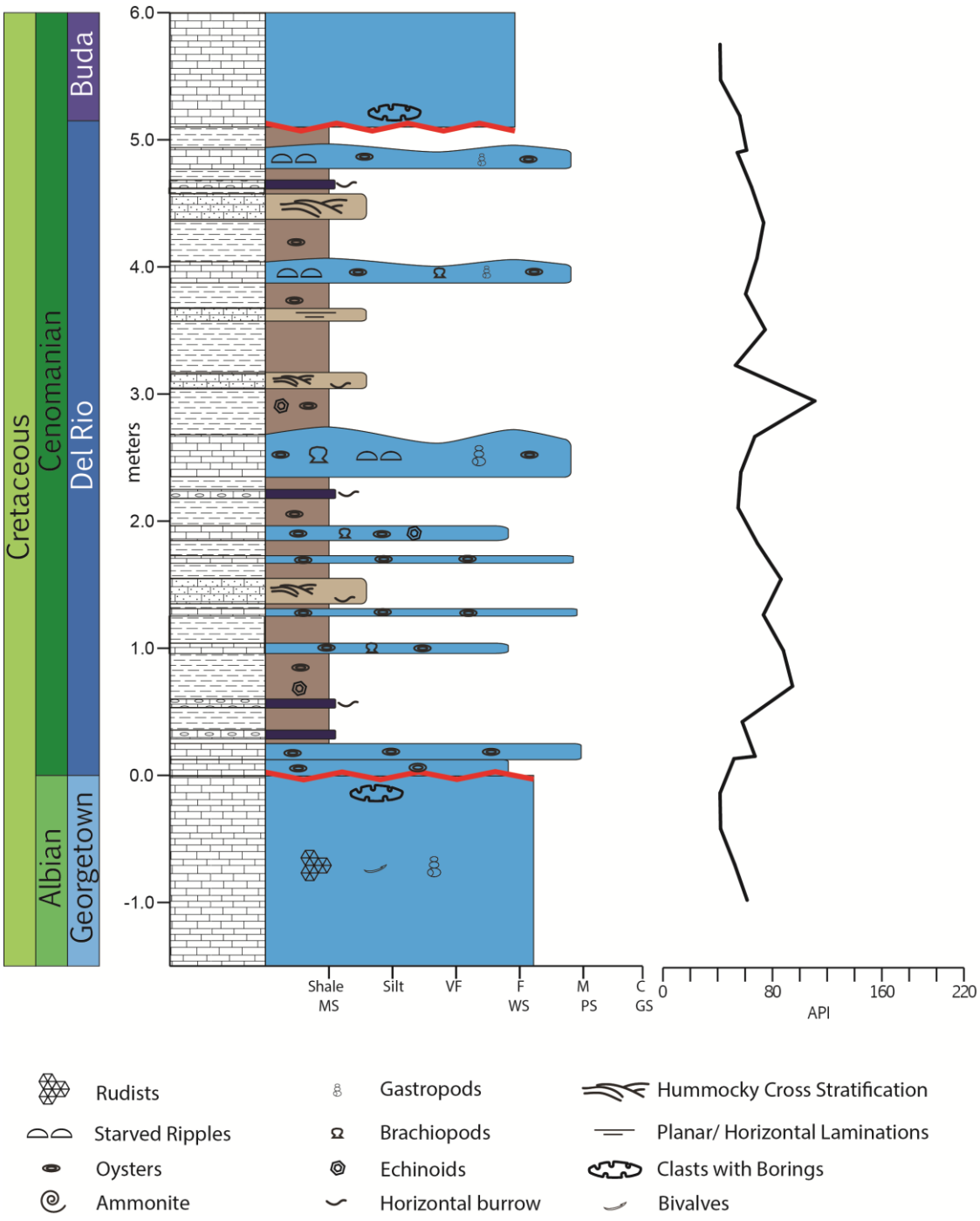

Figure 9. East Pecos River measured section displaying random distribution of facies within the Del Rio Formation. No cyclic patterns noted; however, the section is representative of one sequence.

there is a general shallowing upwards trend supported by the increase of silty units and thicker packstone beds near the top of the section (Fig. 9).

4.2 Core Analysis

A description of the core (Fig. 10; Boring ID 12) was used to further assess the facies distribution and thickness variation of the Del Rio Formation southeast of the outcrops, towards the Maverick Basin. The Del Rio Formation was ~20 meters thick in the core, including a missing 1 meter section around 18 meters into the subsurface. All facies in outcrop occur in the core. The lower contact was more of a gradual contact compared to the upper contact. The basal contact of the Del Rio Formation was marked by the first occurrence of sedimentary structures (laminated siltstone beds) interbedded with calcareous shale above the massive limestone of the underlying Georgetown Formation. The upper contact between the Buda and Del Rio formations is easily distinguished by the abrupt change in lithology from light tan to white skeletal wackestone/mudstone to a grey calcareous shale. Borings of intraclasts of the Del Rio Formation within the Buda Formation occur in core and in outcrop and are indicative of the unconformable surface between these two units.

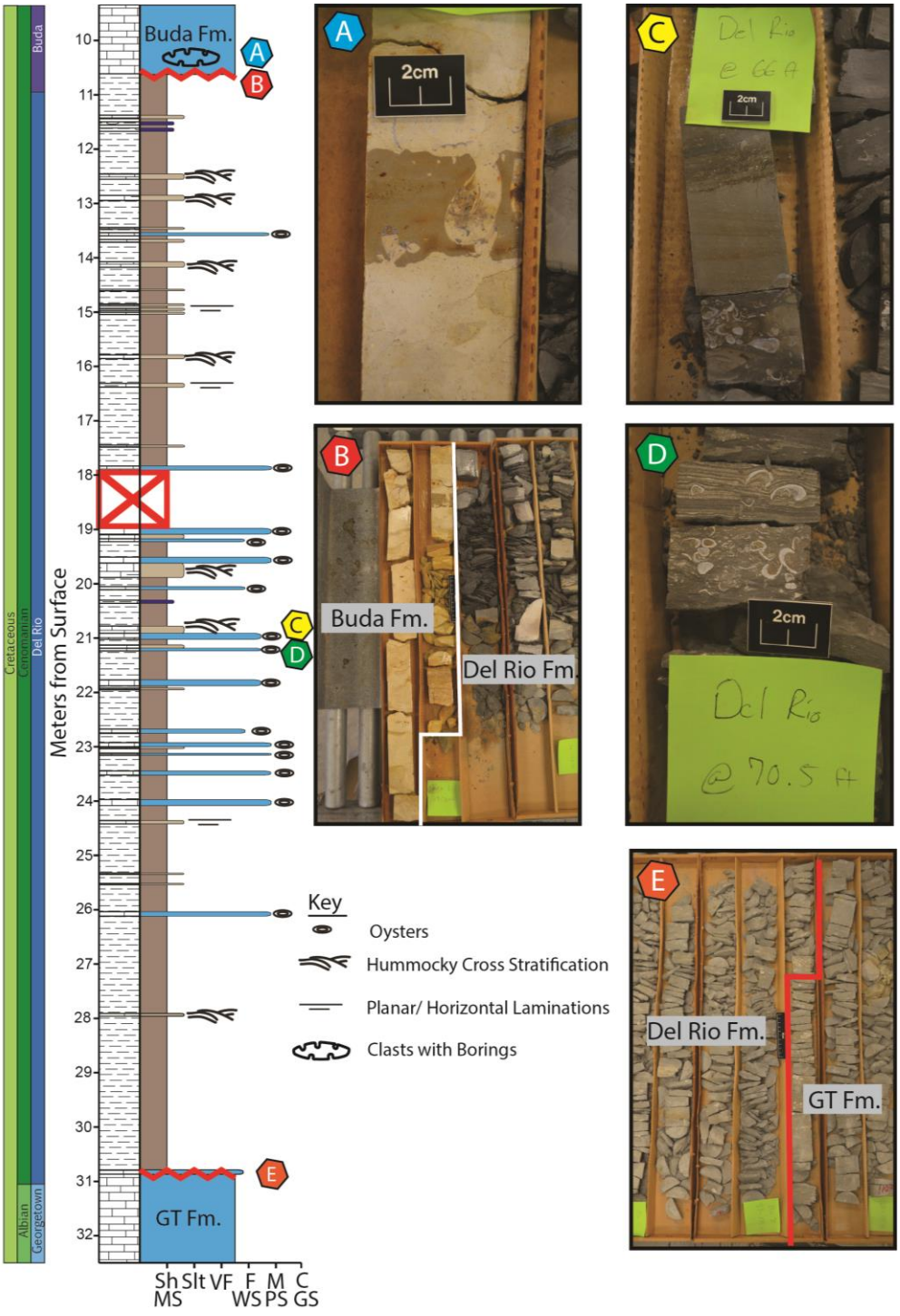

Figure 10. Measured section of Boring ID 12 core including photos of identified facies. A) Del Rio Formation inclusion within the Buda; B) Buda Fm./ Del Rio Fm. contact; C) Laminated silt facies on top of skeletal wackestone; D) Tempestite bedding- packstone base grading into laminated siltstone; E) Del Rio Fm./ Georgetown Fm. contact.

4.3 Thickness Trends

Outcrop thicknesses show a thickening trend to the east and west of the Terrell Arch (Fig. 11). An isopach map of the Del Rio Formation from the 96 wireline logs within the Maverick Basin (Fig. 12) indicates its thickness ranging from 70 ft ~ 270 ft. Although the Del Rio Formation was deposited throughout the Maverick Basin, it thins to the east, being thickest in Maverick County (257 ft or 78 m). The Del Rio Formation thins to the southeast in proximity to the Edwards Reef Margin as well as to the northwest towards the Terrell Arch. “Bullseye” anomalies on the isopach map could have been the result of paleotopography created by the underlying Georgetown Formation or a result of widely distributed data in the study area and gridding algorithm properties.

A wireline log cross section of the Del Rio Formation was generated to correlate outcrop gamma ray logs with subsurface wireline gamma ray logs (Fig. 13). Cross section B-B’ is hung on the Buda Formation in order to analyze thickness trends of the Del Rio Formation along a transect dipping towards the underlying Edwards reef margin to the southeast. The cross section shows that there is a drastic increase of thickness to the southeast in the subsurface of the Maverick Basin, but the formation thins at the southeastern most portion of the map, closer to the underlying Edwards Reef Margin.

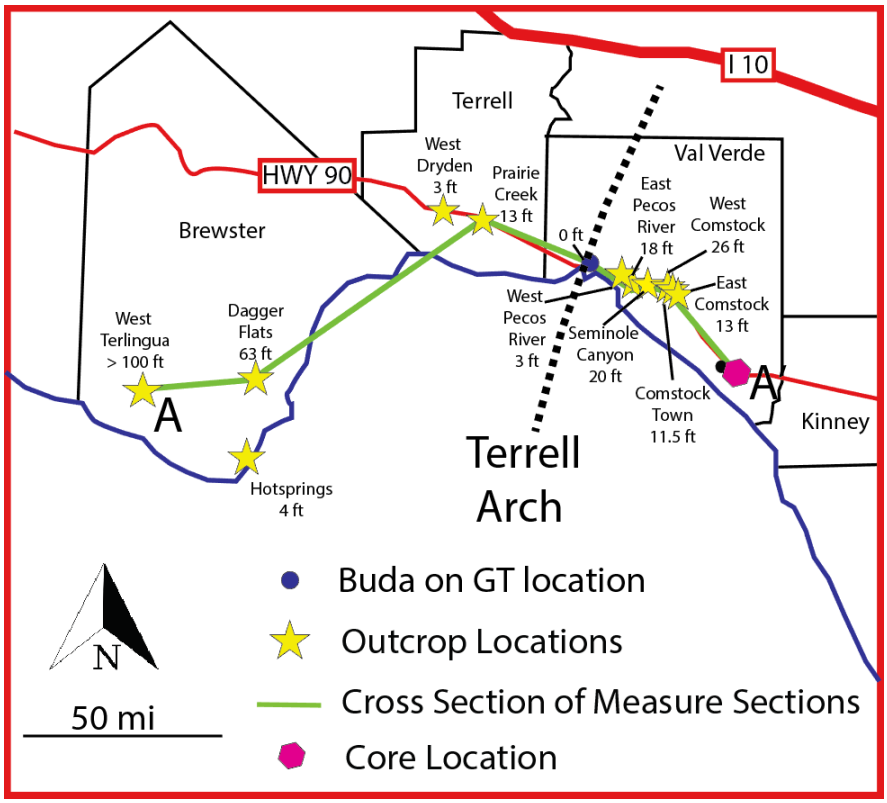

Figure 11. Map of Del Rio Formation outcrops displaying measured thickness

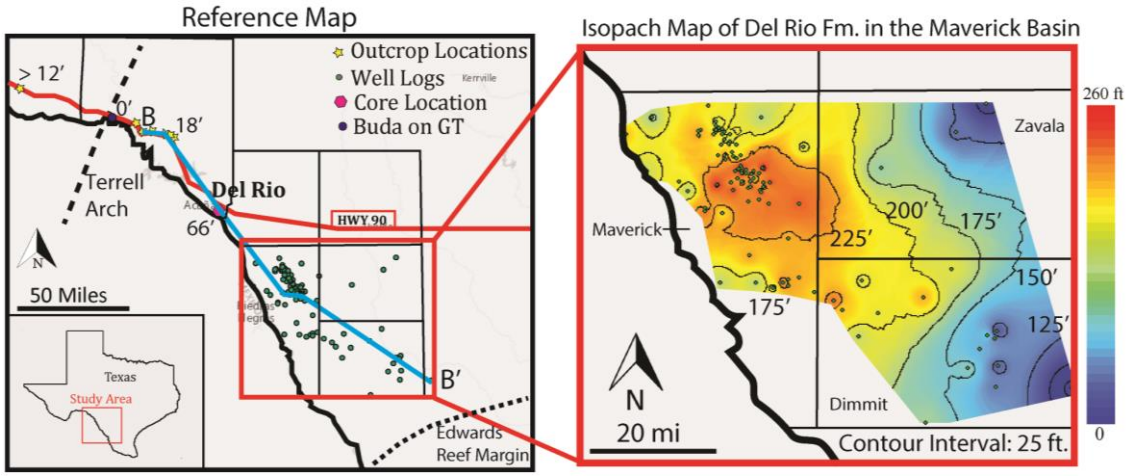

Figure 12. Reference map and isopach of the Del Rio Formation in the Maverick Basin, west Texas

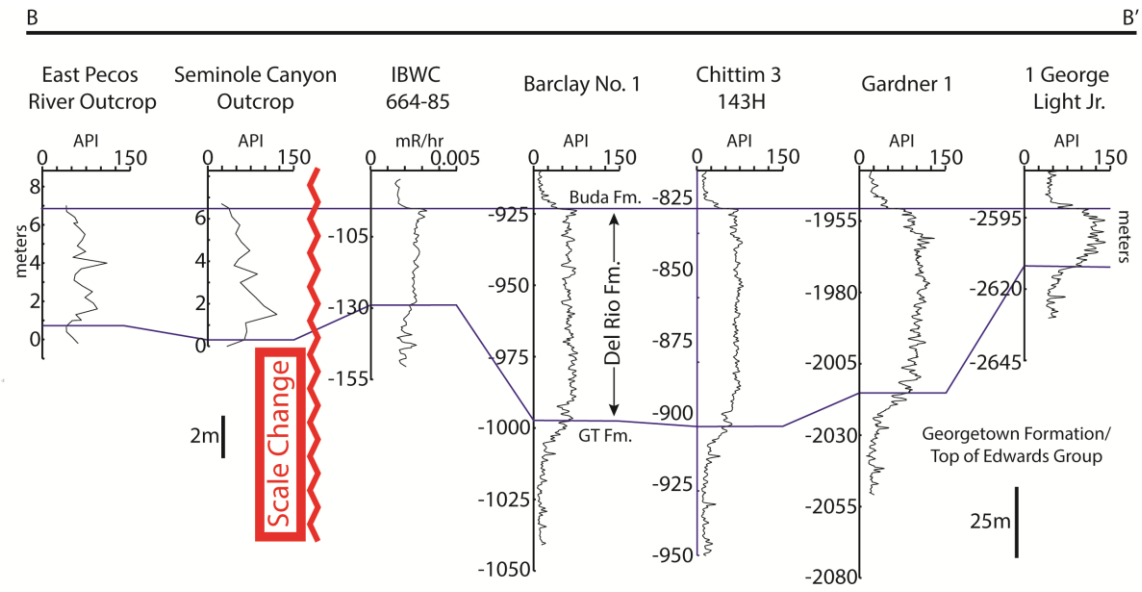

Figure 13. Cross section of outcrops and well logs. Cross section correlating outcrop gamma ray log with subsurface wireline gamma ray log. IBWC 664-85 is representative of the core from the water well Boring ID 12. Barclay No.1, Chittim 143H, Gardener 1, and 1 George Light Jr. are representative of logs used within the Maverick Basin. B-B' transect located on Fig. 12. Note scale change between the outcrops (to the left) and subsurface (to the right).

4.4 Detrital Zircon Results

The detrital zircon geochronology results (Appendix C) are plotted on relative probability plots (Fig. 14) that assess the reliability of the age data by comparing U/Pb ages and their respected errors. Therefore, if each grain in a group of similar age has a low error, that group will plot as a high peak on the probability chart, whereas groups of similar age grains with large errors will have a low peak. Most importantly, the probability plot illustrates the modal age spectra of the source areas that supplied siliciclastic grains to the study area during the Cretaceous. The precision of the dating for both samples averaged 5-8%.

Sample EC1b from the East Comstock outcrop has 117 individual zircon grains with concordant detrital-zircon ages (Fig. 14). Zircon U/Pb isotope data are displayed on a relative probability plot showing the distribution of zircon ages. The age data reveals a mixed distribution of age populations ranging from as young as ~99 Ma to as old as ~2000 Ma. Four age populations constitute a major percentage of the sample and include Lower Cretaceous (99-108 Ma), Mid Paleozoic (350-500 Ma), Cambrian/ Neoproterozoic (500-650 Ma) and Mesoproterozoic- Neoproterozoic (920-1300 Ma) grains. Forming a relatively minor percentage of the age populations are Early Jurassic (171 Ma) grains. In this sample there was one grain with a Neoarchean age (2700 Ma) that was not plotted.

Sample WC2b has 101 individual zircon grains with concordant detrital-zircon ages displayed on a relative probability plot showing the distribution of zircon ages (Fig. 14). The age spectra of this sample has a mixed distribution of age populations ranging as young as ~99 Ma to as old as ~1860 Ma, similar to EC1b. Three age populations constitute a major percentage of the sample and include Lower Cretaceous (99-108 Ma), Middle-Early Paleozoic (350-500 Ma), and Mesoproterozoic-Neoproterozoic (920-1300 Ma) grains. Forming a relatively minor percentage of the age populations are Early Jurassic (171 Ma), and Late Neoproterozoic (600 Ma).

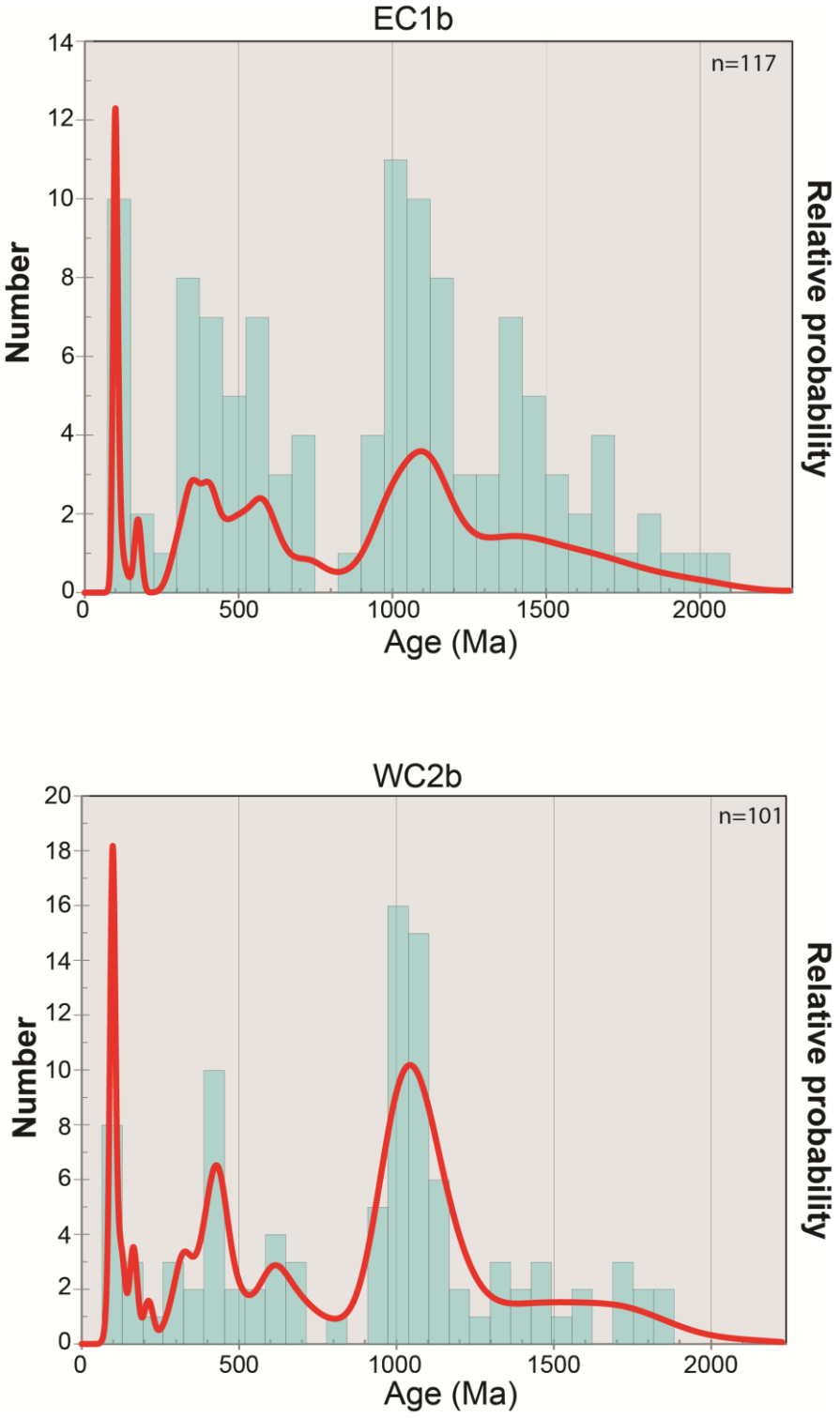

Figure 14. Relative probability plot, samples WC2b and EC1b, Del Rio Formation near Pecos River, west Texas.

5. DISCUSSION

5.1 Depositional Setting

Del Rio Formation lithologies in west Texas are grouped into six sedimentary facies (Fig. 15) that were deposited in shallow, subtidal marine environments within storm wave base (<40 m water depth). Facies A (nodular mud limestone) is interpreted to be the shallowest facies due to high amounts of bioturbation, burrows, massive bedding, and rare, very fine quartz grains (Figs. 15A and 15B). The highly oxygenated waters in shallow marine environments facilitate a productive and active environment for organisms, leading to a greater amount of bioturbation and destruction of internal bedding or sedimentary structures.

Facies B (shallow marine sandstone) and Facies C (marine siltstone) are interpreted to be shallow water facies as well, due to the presence of coarser siliciclastic grains (quartz) and preserved hummocky crossbedding in these units. These two facies also have less bioturbation than Facies A, potentially indicating a slightly deeper more oxygen-depleted environment than Facies A. Facies B is contains very-fine to fine siliciclastic grains, predominantly quartz (Figs. 15C and 15D). Facies B contains the largest siliciclastic grains within the Del Rio Formation and is interpreted to be a shallow marine sandstone deposit, potentially a sheet-flood deposit within tidal environment based on the presence of horizontal laminations, well sorted and rounded grains, thin bedding, and confined locations. Facies C is of silt sized siliciclastic grains (50%) and a calcareous mud matrix (50%) (Figs. 15E and 15F). The hummocky cross-stratification

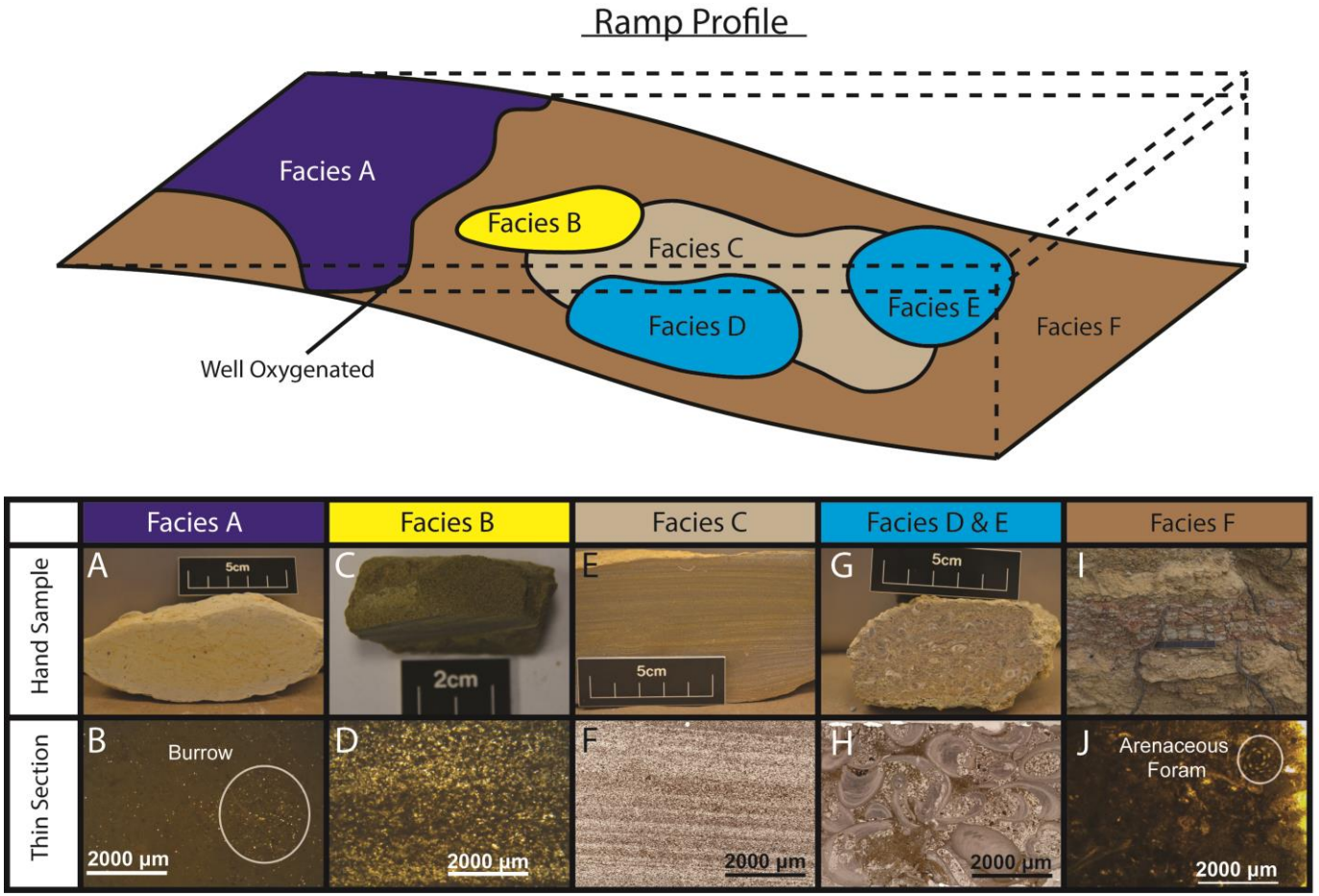

Figure 15. Ramp profile diagram. Simplified ramp diagram of the depositional ramp profile during the Cenomanian displaying the interpreted facies of the Del Rio Formation and their relative depositional water depth. A) Hand sample photo of lime mud nodule (Facies A). B) Thin section of Facies A, displaying interpreted burrow. C) Hand sample photo of very fine sandstone (Facies B). D) Thin section of very fine grained sand sample. E) Hand sample photo of lime siltstone displaying hummocky cross stratification. F) Thin section of laminated lime silt stone (Facies C). G) Hand sample photo of skeletal packstone (Facies D). H) Thin section of skeletal packstone (Facies D) displaying oysters (*I. arietina*). I) Field photo from the East Comstock outcrop showing the calcareous shale (Facies F). J) Thin section of Facies F displaying an Arenaceous Foram.

within Facies C indicates deposition in shallow water during period of high energy needed to create these cross-bedded structures. The siltstone beds are interpreted to be tempestites that formed from combined flows generated by storm waves (Myrow et al., 2001). Tempestites within Facies C are further characterized by graded bedding from a basal thin packstone/ wackestone layer containing horizontal burrows/ tool marks to a silty, hummocky cross stratified interval of silt sized carbonate particles (Lock, 2009).

The skeletal packstone and wackestone facies (Facies D & E) are interpreted to have formed in deeper water along the carbonate ramp but still within shallow water above the storm wave base due to the presence of starved ripples within this facies (Allen, 1982; Boersma, 1969). The mega ripples in the skeletal packstone facies are interpreted to have formed in a deeper facies, because the ripples are bounded on either side by calcareous shale, indicating that this environment contains much shale and that the ripples were generated by infrequent high-energy events, such as storms. The skeletal packstone and wackestone are composed mainly of oysters (*I. arietina*) (Table 1) indicating potential brackish water conditions (Lock, 2009) (Figs. 15G and 15H). These fossiliferous beds resulted from the winnowing of fine material by strong currents or storms, leaving a concentration of oyster shells and other organisms (Lock, 2008). The occurrence of both benthic and planktonic forams within these facies indicates a neritic open marine environment (Mancini, 1977).

Facies F (lower ramp calcareous shale deposit) is interpreted to be the deepest water facies due to the lack of siliciclastic grains and sedimentary structures. This shale is the dominant lithofacies within the Del Rio Formation and contains few scattered

fossils including oysters, echinoids, bivalves, and forams (Figs. 15I and 15H). Though it is fossiliferous, this shale facies is inorganic, containing little to no kerogen. Preservation of organic matter within a shale unit requires a calm and quiet depositional environment, contradictory to the storm dominated carbonate shelf on which the Del Rio Formation was deposited. Facies F was previously interpreted as a lower energy near shore deposit (Lock et. al., 2007). However, this shale facies occurs above and interbedded with every other facies and was deposited across the entire ramp in shallow and deeper water settings.

The sedimentary facies and sedimentary structures indicate that the Del Rio Formation was deposited on a homiclinal ramp composed of mixed siliciclastic and carbonate sediments (Fig 15). A ramp model is indicated by the abundance of preserved storm deposits, and variability of facies and bedding among the outcrop sections. The absence of amalgamated or regionally consistent bed forms, such as thick boundstones or reef complexes, associated with rimmed shelf deposits also indicates a ramp setting as well.

While the lithologies and sedimentary structures of the interpreted facies remain the same across the study area, small-scale parasequences (meter-scale cycles) of shallowing upwards trends or cycles of facies within the Del Rio Formation measured sections were unresolvable. General patterns of shallowing upwards, such as an increase in siltstone facies coupled with thicker packstone beds towards the top of the section, occur in some outcrops (east Pecos River, east Comstock, west Comstock), but this trend does not occur in every outcrop (Appendix A). The occurrence of calcareous shale

between every facies and randomness of facies distributions throughout the sections indicate that the parasequences within the Del Rio Formation likely formed by autocyclic processes. Autocyclicity refers to the redistribution of sediment within a depositional system as a result of processes within the sedimentary system, such as a channel (Beerbower, 1964). Autocyclic processes tend to be instantaneous geologic events that are random and aperiodic, such as storms. Autocyclic processes involve local changes in energy, and therefore, the chemical sedimentology of the regional facies remains the same (Blaine, 2003). Shallow marine settings, such as the interpreted depositional environment of the Del Rio Formation, are more readily affected by internally produced disturbances in sediment deposition and production (Blaine, 2003). Because of the abundance of storm deposits, susceptibility of disturbances within a shallow marine environment, randomness of facies distributions, and inability to resolve sequence patterns within the measured sections, the parasequences within the Del Rio Formation are interpreted to be autocyclic (Fig. 15).

Regional interpretations suggest the Del Rio Formation was deposited during a time of low sea level, with abundant periodic influx of very fine grained siliciclastic grains onto a pre-existing carbonate shelf. This mixed siliciclastic and carbonate sedimentation provides a stark contrast to both the underlying carbonate-rich Georgetown Formation and overlying carbonate Buda Formation. The Del Rio Formation most likely records a long-term sea level lowstand following deposition of the Georgetown Formation sediments and prior to the late Cenomanian transgression that deposited the Buda, Eagle Ford, and Austin Chalk formations (Lock et al., 2007). The

Del Rio Formation is interpreted to be an unconformity-bounded sequence in west Texas (Lock et al., 2007). Clasts with borings and near-surface discoloration at the Del Rio Formation/ Georgetown contact at East Pecos River and Seminole Canyon outcrops indicate an unconformity separating these two units (Lock et al., 2007). Previously, the Del Rio and Buda formations were grouped into a single Transgressive- Regressive sequence (Mancini & Scott, 2006; Mauldin, 1985). However, in both outcrops and core (Fig. 9) the base of the Buda Formation contains extensively bored clasts of the Del Rio Formation. These intraclasts are indicative of an unconformity separating the Del Rio and Buda formations. Therefore, the Del Rio Formation is interpreted to an unconformity-bounded lowstand sequence.

5.2 Thickness Variations

In the study area, the Del Rio Formation of varies in thickness from over 100 feet in the Terlingua West outcrop, west of Big Bend National Park, to 4- 63 feet within the park at the Hot Springs outcrop and Dagger Flats outcrop locations, respectively (Fig. 11). East of the park, the Del Rio Formation thins and is absent on top of the Terrell Arch where the Buda Formation unconformably overlies the Georgetown Formation. The Terrell Arch is a wide, shallow Paleozoic structure oriented roughly north-south from the northeastern Coahuila, Mexico, through Brewster and Terrell counties along the trend of the Del Sierra del Carmen ranges (Alvarez, 1949). East of the Terrell Arch, along highway 90 in Val Verde County, the Del Rio Formation is 18-20 feet at the East Pecos River Outcrop and Seminole Canyon outcrops. Farther south of these outcrops,

cored sections and wireline logs of water wells (Boring ID 12 and IBWC 664-85) record a Del Rio Formation interval of 70 feet in southern Val Verde and Kinney Counties (Fig. 13) Farther south, in Maverick, Dimmit and Zavala counties, the Del Rio Formation varies in thickness from 70-260 feet in wireline logs in the Maverick Basin (Figure 12 and 13).

The variable thickness of the Del Rio Formation is interpreted to be a combination of onlap of the formation against pre-existing topography of the Lower Cretaceous Edwards platform, and erosion beneath the Buda Formation (Lonsdale et al., 1955). The Del Rio Formation thins toward the Terrell Arch, but the arch potentially affected more than just thickness of the unit. The outcrops on both sides of the arch share the same lithofacies and sedimentary structures (storm deposits); however, the outcrops to the west of the Terrell Arch lack the quantity of skeletal packstone and siliciclastic facies common in the outcrops east of the arch (Fig. 8). The Terlingua and Dagger Flats outcrops lack the common oyster (*I. arietina)* that are prevalent east of the arch. *I. arietina* is more abundant in the lower section of the Del Rio Formation (Maxwell and Dietrich, 1972). Thus, outcrops west of the Terrell Arch may record an upper, younger section of Del Rio Formation. Alternatively, the structural high of the Terrell Arch may have substantially impeded sediment transport to the west, and therefore, the depositional environment that produced the sandstone and siltstone beds to the east did not reach west of the arch (Lock et al., 2007). Additionally, the gamma ray values are significantly higher in outcrops west of the Terrell arch, averaging values ranging from 100-110 API units. The outcrops east of the Terrell Arch typically average gamma ray

values 80 API units. This increase in the gamma ray signature is interpreted to correlate with the loss of the coarser grained facies (sandstone, siltstone, and packstone) and increased shale.

There are major differences between the Del Rio Formation and its lateral equivalent, the Grayson Formation, northeast of the San Marcos Arch in central Texas. The Grayson Formation is predominantly a calcareous shale that is much more clay-rich than the Del Rio Formation of west Texas (Mancini, 1977). The uniform, unbedded, silty claystone of the Grayson Formation contrasts the calcareous shale section full of skeletal packstone, wackestone, and siltstone interbeds of the Del Rio Formation across the San Marcos Arch. The Grayson Formation also has uniform thickness (80-100 feet) throughout central Texas but thickens in the subsurface towards the Stuart City Reef Margin to about 170 feet (Mancini, 1977). Due to the more consistent lithologies and thicknesses and lack of HCS in the Grayson Formation, we infer that its depositional environment was less affected by storms than the Del Rio Formation.

Cretaceous strata, including the Del Rio Formation, Buda Limestone, Eagleford Shale, and Austin Chalk, tend to be abnormally thick within the Maverick Basin. This increase in formation thickness is a possible indicator of basinal depression creating the needed accommodation space for the sediments. Recent seismic surveys show that the accommodation space within the basin is likely due to a northwest- southeast trending rift zone made up of a series of half-grabens (Scott, 2004). It is interpreted that these half grabens resulted from a failed rift during the opening of the Gulf of Mexico in the

Jurassic and serves as the structural control for the depression and sediment accumulation of the Maverick Basin (Scott, 2004).

5.3 Provenance

Extensive research has focused on Del Rio Formation sediment provenance. Matching the detrital zircon age populations of a sample with known provenance ages is an effective way to understand sediment supply to basins within a certain time interval (e.g. Soreghan and Soreghan, 2013; Gehrels et al., 2011; Moecher et al., 2011; Vega-Granillo et al., 2008; Gleason et al., 2007) . Potential provenance areas for the detrital zircons analyzed in the Del Rio Formation are grouped into five approximate age populations: Late Mesoproterozoic to Early Neoproterozoic (900-1300 Ma), Neoproterozoic/ Cambrian (500-650 Ma), Middle Paleozoic (350-500 Ma), Jurassic (170-175 Ma), and Middle Cretaceous (99-100 Ma).

5.3.1 Mesoproterozoic/ Early Neoproterozoic (900-1300 Ma)

Zircons reflecting a Mesoproterozoic to Early Neoproterozoic age range are linked to the Grenville Orogeny, a mountain building event that resulted from the assembly of Rodinia, specifically from the convergent margins of the continental collision of eastern and southern Laurentia (Hoffman, 1991; Gleason et al., 2007). Zircon ages corresponding with the crystallization of the Grenville orogeny (~900 - 1350 Ma) are very common in detrital zirxon samples of late Paleozoic and Mesozoic sediments of North America (Soreghan and Soreghan, 2013; Moecher and Samson,

2006; Gleason et al., 2007; Gehrels et al., 2011). Granitic intrusions that crystallized during the Grenville Orogeny within Laurentia are extremely zircon-rich and laterally extensive, spanning several cratons including eastern and central North America as well as parts of Mexico and Gondwanan continents (Moecher and Samson, 2006). The Grenville population has a strong presence within the Appalachian strata record and is reflected as a dominant presence within modern-day fluvial systems of the Appalachians. The Ouachita Orogeny and Marathon uplifts also contain a prominent Grenville population that is most likely due to recycled sediments derived from the Appalachian Orogeny and Gondwanan continental crust (Gleason, 2007).

A more proximal source for the Grenville-age sediments within the Del Rio Formation would be the Llano Uplift in central Texas. The basement rocks of the Llano Uplift are Grenville-age (1000-1300 Ma) granitic plutons and metamorphic sediments (Walker, 1992).

5.3.2 Neoproterozoic/Cambrian (500-650 Ma)

Neoproterozoic-Cambrian zircons are common in the Del Rio Formation (Fig. 13). Neoproterozoic igneous and metamorphic rocks occur in terranes that were exposed due to the convergence of Gondwana and Laurentia (290 to 310 Ma), coupled with the uplifting of the interior Appalachian Orogeny during the Late Paleozoic (Soreghan and Soreghan, 2013). These uplifted units provide zircons ages ranging from 515-760 Ma and include the Avalon terrane in the northern Appalachians, the Carolina terranes in the southern Appalachians, and Suwannee terrane in the Florida subsurface (Dickenson and

Gehrels, 2003; Soreghan and Soreghan, 2013; Mueller et al., 1994; Moecher et al., 2011). The Neoproterozoic rocks in the Blue Ridge are rift related volcanic and plutonic rocks (Crossnore plutonic volcanic complex, Robertson River granites, Bakersville mafic intrusive suites; Catoctin and Mount Rogers volcanics) with ages ranging from 550-765 Ma (Moecher et al., 2011; Goldberg et al., 1986; Su et al., 1994).

Another possible source for Cambrian grains are the igneous rocks in the Ancestral Rocky Mountains (ARM) throughout southern Colorado and New Mexico. These rocks have mafic and felsic compositions and record ages ranging from 427-574 Ma in southern Colorado and 457-664 Ma in New Mexico (McMillan and McLemore, 2004). The Wichita Uplift is another ARM related terrane located in Oklahoma with grains aging from 527-536 Ma (Hames et al., 1998). However, the basement rocks exposed during periods of erosion within the ARM are principally composed of Paleoproterozoic (1600-1825 Ma) grains (Soreghan and Soreghan, 2013). Yet, in the Del Rio Formation, only 12 grains from sample EC1b (11%) and 9 grains from sample WC2b (9%) have ages greater than 1600 Ma. Additionally, the erosion rates within these uplifted ARM source terranes had substantially decreased during the Middle Permian due to onlap of Early Permian strata, and were likely not exposed during the Cretaceous (Soreghan and Soreghan, 2013, Gehrels et al., 2011).

Additionally, Gondwanan units occur in the Yucatan-Maya and Coahuilla terranes in Mexico and Central American that were uplifted during the collision between Gondwana and Laurentia contain Cambrian/ Neoproterozoic aged grains. These source

rocks include the Yucatan-Maya terrane and Coahuilla terrane. Detrital zircon ages from these rocks range from 500-650 Ma (Weber et al., 2006), but the precise location of these Central American Gondwanan terranes is unknown (Dickinson and Lawton 2001; Murphy et al. 2004; 59 Vega-Granilo et al. 2008; Martens et al. 2010). However, since these terranes were involved with the collisional event that formed Pangea, they could have supplied the Ouachita/ Marathon system with Neoproteroizoic/Cambrian aged sediments (Soreghan and Soreghan, 2013). Sediments derived from the Ouachita Orogeny reflect recycled sediment from Appalachian and Gondwanan terranes, therefore the Ouachitas are a viable source for Neoproterozoic/Cambrian grains (Gleason et al., 2007).

5.3.3 Middle Paleozoic (350-500 Ma)

Zircons corresponding with the Middle Paleozoic (350-500 Ma) can be correlated to multiple different source areas within North America. The Appalachian Orogeny contains units reflecting the Middle Paleozoic period including the Taconic (440-490 Ma) and Acadian (350-420 Ma) orogenies (Miller et al., 2000; Soreghan and Soreghan, 2013). The Taconic and Acadian orogenies were the first two mountain-building events following the Late Neoproterozoic/ Early Cambrian rifting (Bradley, 1983).

Paleozoic grains also occur in Mexican Mixteca terrane (440-480 Ma), Yucatan-Maya terrane (418 Ma), and there are metamorphic ages within the Coahuilla terrane (Weber et al., 2006; Keppie et al., 2004). The collision of the Mixteca terrane and

suturing of the Coahuilla and Yucatan-Maya terranes had occurred by the Middle Permian (Martens et al., 2010), however these terranes were actively eroding Paleozoic sediments during the Permian, so whether these sources provided sediment into the Cretaceous is unresolved (Soreghan and Soreghan, 2013).

5.3.4 Jurassic (170-175 Ma)

During the Jurassic, the western plate boundary of North America was colliding against the Pacific oceanic plate along an active subduction zone with multiple volcanic arcs (Michalzik, 1991). The small but persistent Jurassic zircon population among the two Del Rio Formation samples is likely linked to volcanic events that occurred in the western portion of North America during the break up of Pangea in the Early and Middle Jurassic. From 200-155 Ma, magmatism was extensive along the North American Cordilleran range in the Wrangle, Quesnal, Stikine, and Yukon terranes (Armstrong, 1988). Sediment shed from these northwestern terranes could have traveled southeasterly through river systems along the western margin and into the developing Gulf of Mexico or ash from its volcanoes populated nearby settings.

5.3.5 Middle Cretaceous (99-100 Ma)

The zircon ages corresponding with the Middle Cretaceous are most likely related to volcanic activity during or immediately preceding deposition of the Cenomanian Del Rio Formation. The Cretaceous Sevier Orogeny was a major volcanic event in North America. Produced by the subduction of the Farallon plate beneath the North American continental plate, beginning approximately 140 Ma and ending 50 Ma

(Yonkee, 2015). During the Cenomanian, the rate of convergence between the Pacific oceanic plate and North American plate and magnetism within the Sierra Nevada arc increased, which in turn drove the crustal shortening associated with the Sevier fold and thrust belt (Yonkee, 2015). The Sevier Orogenic belt has a history of deformation throughout the Cretaceous and provided siliciclastic sediment east of the Cordilleran Margin (Armstrong, 1988), and potentially contributed to the siliciclastic composition of the Del Rio Formation.

5.3.6 Provenance Discussion

The detrital zircon spectrum for the two Cenomanian Del Rio Formation samples are very similar and both indicate multiple potential sources. Based on the age populations, siliciclastic grains within the Del Rio Formation are interpreted to be an amalgamation of different provenances. These sources include the Appalachian and Ouachita orogenies (Gondwanan terranes), as well as western volcanic arcs during the Jurassic, and the Cretaceous Sevier orogeny.

The Appalachian Orogeny is a potential source of siliciclastic grains for the Del Rio Formation because of its well-defined Paleozoic and Grenville aged events (Moecher et. al, 2011; Soreghan and Soreghan, 2013). The Appalachian Orogeny has a characteristic detrital signature consisting of a significant Grenville and Paleozoic age (Taconic and Acadian orogeny) populations (Moecher and Samson, 2006; Gehrels et al., 2011) (Fig. 16). Sample EC1b contains a dominant Grenville aged population (51% of the total zircon age spectra) and a prominent Middle Paleozoic peak as well (19% of the total zircon age spectra). Sample WC2b also contains a dominant Grenville aged

population (48% of total zircon age spectra) and a prominent Paleozoic presence (17% of total zircon age spectra). The French Broad alluvium system in the Blue Ridge terrain (Southern Appalachians) contains a dominant Middle Ordovician aged zircon population (450 Ma), with secondary populations occurring at 1150–1190 and 1000–1050 Ma (Moecher et al., 2011). Neoproterozoic ages are not as abundant Mesoproterozoic ages, but still present within the French Broad alluvium zircon spectrum. Additionally, Grenville aged granitoids in the Appalachians have an abnormally high zircon fertility rate and were proposed to be the most significant source of Grenvillian-age zircons to depocenters across North America (Gleason et al. 1995; Moecher and Samson, 2006). Thus, the Appalachians are a likely source for the Mesoproterozoic- Early Neoproterozoic and Middle Paleozoic sediments within the Del Rio Formation (Figs. 16 and 17). However, the Appalachian Orogeny (Fig. 15) lacks the necessary abundance of Late Neoproterozoic/Cambrian grains (Moecher et al., 2011).

The Ouachita Orogeny and Marathon Uplift is another viable contributor of siliciclastic grains for the Del Rio Formation (Stewart et al., 1999). The detrital zircon record of the Ouachita and Marathon systems is very similar to that of the Appalachian Orogeny due to the recycling of Appalachian detritus and Gondwanan sediment within Ouachita strata (Thomas et al., 2004; Gleason et al., 2007). A distributed pattern of Neoproterozoic/Cambrian (510-790 Ma) and Middle Paleozoic (285-490 Ma) ages is common in Ouachita derived sediments (Fig. 16) as seen in the Pennsylvanian Haymond Formation and Chinle-Dockum fluvial system (Gleason et al., 2007; Dickenson et al., 2010). The Neoproterozoic/ Cambrian and Middle Paleozoic grains within the

Ouachita/Marathon system were likely derived from the Peri-Gondwanan Yucatan-Maya and Coahuilla terranes (500-600 Ma) as well as the Taconic and Acadian Orogenies from the Appalachian Orogeny. A Grenville peak also occurs in Ouachita sediments and could have been derived from recycled zircon rich Appalachian basement rock or crustal blocks of the Godwanan plate during the collision with Laurentia. The Ouachita Orogeny detrital spectrum (Fig. 16) also contains a population of grains older than 1300 Ma (Gleason et al., 2007). These older ages are reflected in the Del Rio Formation samples, taking up approximately 15-20% of the total population of grains (Fig. 14). Therefore, since the Ouachita and Marathon system contains all age populations in the Del Rio Formation, it is interpreted to be a more viable source of siliciclastic grains for the Del Rio Formation than the Appalachian Orogeny (Figs. 17 and 18). Additionally, the Llano Uplift (1000-1300 Ma) is a viable local source contributing additional Grenville aged sediments (Fig. 18) to the Del Rio Formation (Walker, 1992).

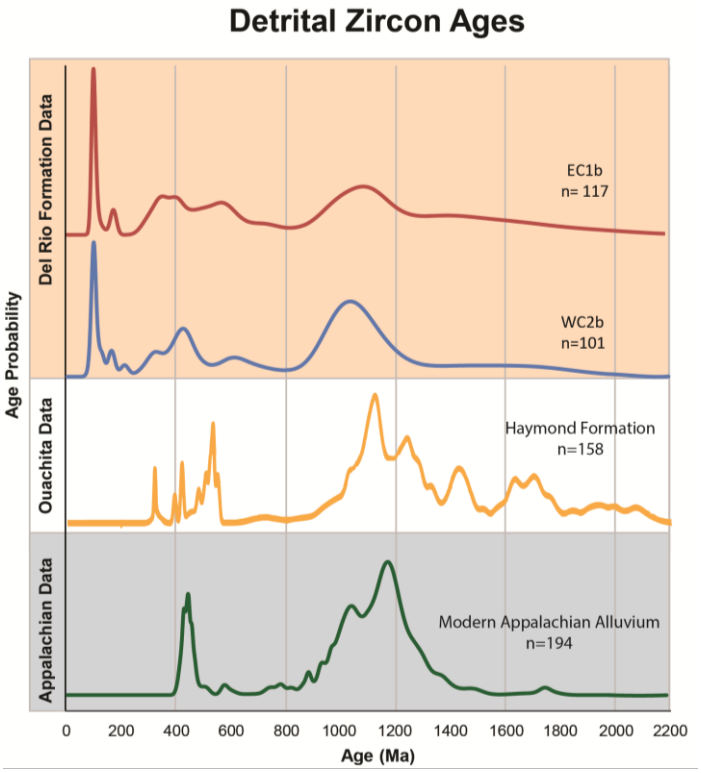

Figure 16. Probability density plots of the Del Rio Formation samples, and other formations derived from the Appalachian or Ouachita Orogenies. Detrital signature for the Pennslyvanian Haymond formation is from Gleason et al. (2007). The detrital signature for the Modern Appalachian Alluvium is by Moecher et al. (2011).

The Jurassic peak within the Del Rio Formation detrital spectrum is interpreted to be sourced from the volcanic arcs along the western continental plate boundary of North America, specifically from the North American Cordillera (Fig. 17). Volcanism was also active along the western margin of modern day Mexico, but disregarded as a sediment source because it is unlikely that sediment would travel north across the topographic low of the basin (Fig. 18) and be deposited into the study area (Martini, 2016). Therefore, the subduction zone and island arcs of the western United States are

the only viable location for Jurassic zircons in the Del Rio Formation (Fig. 17). Similarly, the Cretaceous grains in the Del Rio Formation detrital record are interpreted to have been derived from the Sevier Orogeny due to the lack of volcanic activity anywhere else in North America during the Cretaceous (Figs. 17 and 18). Both the Cretaceous and Jurassic zircons could have used similar pathways, such as rivers or streams, as transport systems into the study area.

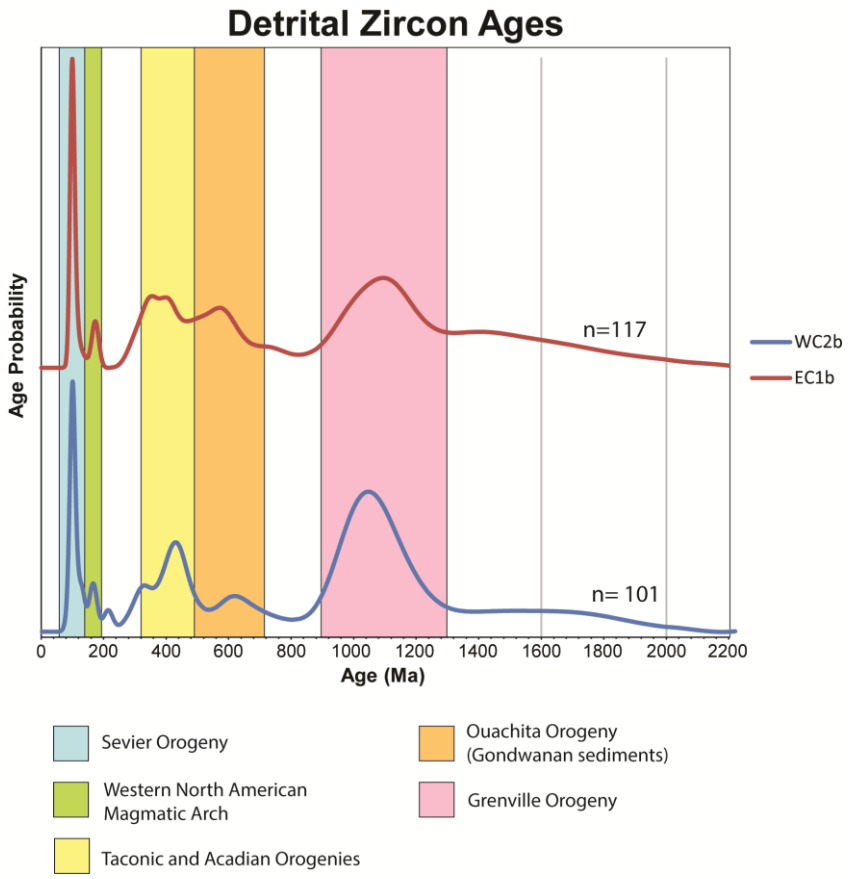

Figure 17. Probability density plots for Del Rio Samples EC1b and WC2b with interpreted provenance.

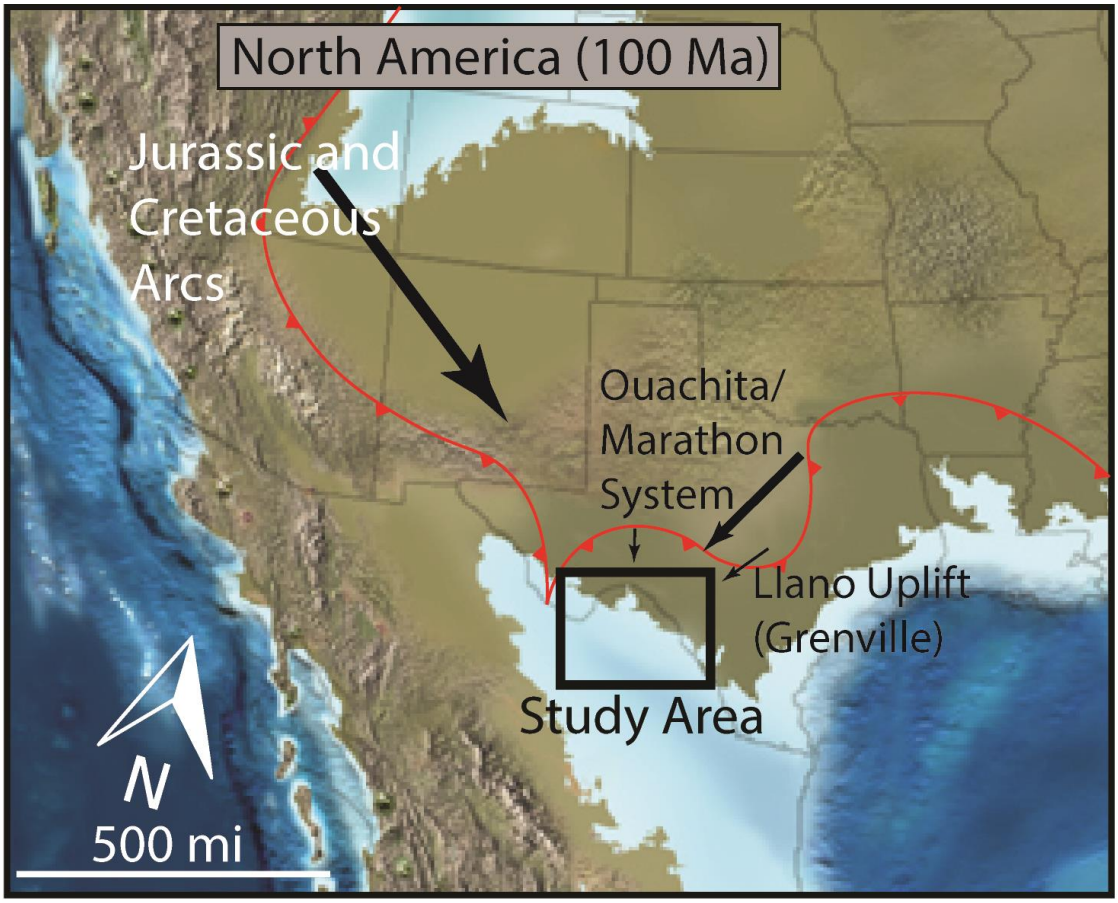

Figure 18. Modified Blakey map of North America (100 Ma), displaying the direction of sedimentation of viable sediment sources (from Blakey, 2015).

6. CONCLUSIONS

Outcrop data, hand samples, thin sections, core descriptions, wireline logs, and detrital zircons of the Del Rio Formation across the Maverick Basin and west Texas provide a clearer picture of its regional stratigraphy, thickness variations, provenance and depositional environments.

1. The lithologies of the west Texas Del Rio Formation are grouped into six facies that indicate deposition occurred in a shallow, subtidal marine environment within storm wave base. The facies and their sedimentary structures indicate the Del Rio Formation was deposited on a homiclinal ramp that records alternating carbonate and siliciclastic deposition. A ramp model is indicated by the abundance of preserved storm deposits, variability of facies, lack of reef facies and little or no evidence of shelf break.
2. The Del Rio Formation is interpreted to be a lowstand systems tract. The Del Rio Formation sequence records an overall shallowing trend, but small scale cycles cannot be correlated. Depositional cycles within the Del Rio Formation are interpreted to be autocyclic because of the abundance of storm deposits, susceptibility of disturbances within a shallow marine environment, randomness of facies distributions, and inability to resolve sequence patterns within the measured sections.
3. The variable thickness of the Del Rio Formation is interpreted to result from onlapping against pre-existing topography of the Lower Cretaceous Edwards platform, and erosion beneath the Buda. The pre-existing Terrell and San Marcos

Arches not only affected the thickness of the unit, but also the regional depositional settings. The Terrell Arch substantially impeded coarse siliciclastic sediment transport to the west. Also, the coeval Grayson Formation with its the more consistent lithologies and thickness is interpreted to have deposited in a more stable and quiet environment than that of the Del Rio Formation west of the San Marcos Arch.

4. The siliciclastic grains within the Del Rio Formation likely record an amalgamation of several source areas. The most viable sources include the Ouachita Orogeny/ Marathon Uplift (recycled Gondwanan and Appalachian sediments), the Llano uplift, and Jurassic-Cretaceous volcanic arcs to the west.

REFERENCES

Allen, J.R.L., 1982. Sedimentary structures, their character and physical basis: *Developments in Sedimentology*, v.1, p. 593.

Alvarez, M., Jr., 1949. Tectonics of Mexico: *American Association of Petroleum Geologists Bulletin*, v. 53, p. 1319-1335.

Armstrong, R.L., 1968. Sevier orogenic belt in Nevada and Utah: *Geological Society of America Bulletin*, v. 79, p. 429-458.

Armstrong, R.L., 1988. Mesozoic and early Cenozoic magmatic evolution of the Canadian Cordillera: *Geological Society of America Bulletin*, v. 218, p. 55-92.

Becker, T.P., Thomas, W.A., Samson, S.D., Gehrels, G.E., 2005. Detrital zircon evidence of Laurentian crustal dominance in the Lower Pennsylvanian deposits of the Alleghanian clastic wedge in eastern North America: *Sedimentary Geology*, v. 182, p. 59-86.

Becker, T.P., Thomas, W.A., Gehrels, G.E., 2006. Linking late Paleozoic sedimentary provenance in the Appalachian Basin to the history of Alleghanian deformation: *American Journal of Science*, v. 306, p. 777-798.

Blakey, R.C., Peterson, F., and Kocurek, G., 1988. Late Paleozoic and Mesozoic eolian deposits of the Western Interior of the United States: *Sedimentary Geology*, v.56, p. 3-125.

Blakey, R.C., 2008. Pennsylvanian–Jurassic sedimentary basins of the Colorado Plateau and Southern Rocky Mountains, in Miall, A.D., ed., Sedimentary Basins of the World: *Amsterdam, Elsevier*, v. 5, p. 245–296.

Boersma, J.R., 1969. Internal structure of some tidal mega-ripples on a shoal in the Westerschelde estuary, the Netherlands. Report of a preliminary investigation: *Geologie en Mijnbouw*, v. 46, p. 217–235.

Bradey, D.C., 1983. Tectonics of the Acadian Orogeny in New England and Adjacent Canada: *The Journal of Geology*, v. 91, p. 381-400.

Chang, Z., J. D. Vervoort, W. C. McClelland, and C. Knaack, 2006. U-Pb dating of zircon by LA-ICP-MS: *Geochem. Geophys. Geosyst*., v. 7.

Corfu, F., Hanchar, J.M., Hoskin, P.W.O., Kinny, P., 2003. Atlas of zircon textures: *Reviews in Mineralogy and Geochemistry*, v. 53, p. 469-500.

Dickinson, W.R., Lawton, T.F., 2001. Carboniferous to Cretaceous assembly and fragmentation of Mexico: *Bulletin of the Geological Society of America*, v. 113, p. 1142-1160.

Dickinson, W.R., Gehrels, G.E., 2003. U-Pb ages of detrital zircons from Permian and Jurassic eolian sandstones of the Colorado Plateau, USA; paleogeographic implications: *Sedimentary Geology*, v. 163, p. 29-66.

Dickinson, William R., et al., 2010. Late Triassic Texas uplift preceding Jurassic opening of the Gulf of Mexico: Evidence from U-Pb ages of detrital zircons: *Geosphere*, v. 6, p. 641-662.

Droser, M.L.; Bottjer, D.J., 1986. A semiquantitative field classification of ichnofabric*: Journal of Sedimentary Research*, v. 56, p. 558–559.

Eriksson, K.A., Campbell, I.H., Palin, J.M., Allen, C.M., Bock, B., 2004. Evidence for multiple recycling in Neoproterozoic through Pennsylvanian sedimentary rocks of the central Appalachian Basin: *Journal of Geology*, v. 112, p. 261-276.

Fedo, C. M., 2003. Detrital Zircon Analysis of the Sedimentary Record. *Reviews in mineralogy and geochemistry*, v. 53, p. 277-303.

Fisher, W.L., Rodda, P.U., 1969. Edwards Formation (Lower Cretaceous), Texas: Dolomitization in a Carbonate Platform System: *AAPG Bulletin*, v. 53, p. 55-72.

Gehrels, G.E., Blakey, R., Karlstrom, K.E., Timmons, J.M., Dickinson, B., Pecha, M., 2011. Detrital zircon U-Pb geochronology of Paleozoic strata in the Grand Canyon, Arizona: *Lithosphere* v. 3, p. 183-200.

Gleason J.D., Patchett P.J., Dickinson W.R., and Ruiz J., 1995. Nd isotopic constraints on sediment sources of the Ouachita–Marathon fold belt: *Geological Society of America, Bulletin*, v. 107, p. 1192– 1210.

Gleason, James D., et al., 2007. Laurentian Sources for Detrital Zircon Grains in Turbidite and Deltaic Sandstone of the Pennsylvanian Haymond Formation, Marathon Assemblage, West Texas, U.S.A.: *Journal of Sedimentary Research*, v. 77, p. 888-900.

Goldberg, S.A., Butler, J.R., and Fullagar, P.D., 1986. The Bakersville dike swarm: Geochronology and petrogenesis of Late Proterozoic basaltic magmatism in the southern Appalachian Blue Ridge: *American Journal of Science*, v. 286, p. 403–430.

Gray, M.B., Zeitler, P.K., 1997. Comparison of clastic wedge provenance in the Appalachian foreland using U/Pb ages of detrital zircons: *Tectonics*, v. 16, p. 151-160.

Hames, W.E., Hogan, J.P., Gilbert, M.C., 1998. Revised granite-gabbro age relationships, Southern Oklahoma Aulacogen: *U.S.A. Proceedings of the International Conferences on Basement Tectonics*, v. 12, p. 247-249.

Heinselman and Miron, 1996. The boundary waters wilderness ecosystem: *Minneapolis and London, University of Minnesota Press*, p. 334.

Hentz, Tucker F., and Ruppel, StephenC., 2011. Regional Stratigraphic and Rock Characterisitcs of Eagle Ford Shale in Its Play Area: Maverick Basin to East Texas Basin: *AAPG Annual Convention and Exhibition*

Hoffman, P.F., 1991. Did the Breakout of Laurentia Turn Godnwanaland Inside-Out?: *Science*, v. 252, p. 1409.

Holland, S. M., 1997. Cycle Anatomy and Variability in the Storm-Dominated Type Cincinnatian (Upper Ordivician): Coming to Grips with Cycle Delineation and Genesis: *The Journal of Geology*, v. 105, p. 135-152.

Jirsa, M. A., Miller Jr, J. D., Severson, M. J., & Chandler, V. W., 2006. Final Report on the Geology, Geochemistry, Geophysical Attributes, and Platinum Group Element Potential of Mafic to Ultramafic Intrusions in Minnesota, Excluding the Duluth Complex: *University of Minnesota*

Keppie, J.D., Sandberg, C.A., Miller, B.V., Sanchez-Zavala, J.L., Nance, R.D., Poole, F.G., 2004. Implications of latest Pennsylvanian to Middle Permian paleontological and U/Pb SHRIMP data from the Tecomate Formation to redating tectonothermal events in the Acatlan Complex, southern Mexico. *International Geology Review*, v. 46, p. 745-753.

Leckie et al., 1998. Paleoceanography of the Southwestern Western Interior Sea During the Time of the Cenomanian-Turonian Boundary (Late Cretaceous): *Society for Sedimentary Geology*, v. 6, p. 101-126

Lock, B. E., F. S. Bases, and R. A. Glaser, 2007. The Cenomanian sequence stratigraphy of Central to West Texas: *Gulf Coast Association of Geological Societies Transactions*, v. 57, p. 465.–479.

Lock, B. E., 2008. Clay Mineralogy of the Del Rio Clay Formation (Cenomanian), West Texas: Illite/Kaolinite Ratios as Relative Salinity Indicators*: Gulf Coast Association of Geological Societies Transactions*, v. 58, p. 405-524.

Lock, B. E., 2008. Microbial mats on siliciclastic bedding surface—Kinneyia—in the Del Rio Formation (Cenomanian), West Texas: *Gulf Coast Association of Geological Societies Transactions*, v. 58, p. 635–644.

Lock, B. E., R. W. Butler, and R. T. Franklund, 2009. Tempestite sedimentation: An example from the Del Rio Formation of West Texas*: Gulf Coast Association of Geological Societies Transactions,* v. 59, p. 463–476.

Lock, B. E., J. W. Grimball, and J. G. Johnson, 2013. The Cenomanian Del Rio Formation in West Texas: *Gulf Coast Association of Geological Societies Transactions*, v. 63, p. 331.–342.

Lonsdale J. T., R. A. Maxwell, J. A. Wilson and R. T. Hazzard, 1955. Guidebook -1955 Spring field trip, Big Bend National Park, Texas: *West Texas Geological Society, Midland, Texas,* p. 142.

Mattinson, J. M., 2013. Revolution and evolution: 100 years of U–Pb Geochronology: *Elements,* v. 9, p. 53-57.

Mallory, W.W., 1972. Pennsylvanian arkose and the Ancestral Rocky Mountains in Mallory, W.W., ed., Geologic Atlas of the Rocky Mountain Region: *Rocky Mountain Association of Geologists,* v. D2, p. 131–132.

Mancini, E.A., 1977. Depositional Environment of the Grayson Formation (Upper Cretaceous) of Texas: *GCAGS Transactions,* v. 27, p. 334-351.

Mancini, E. A., 1979. Late Albian and early Cenomanian Grayson ammonite biostratigraphy in North-Central Texas: *Journal of Paleontology*, v. 53, p. 1013–1022.

Mancini, E. A., and R. W. Scott, 2006. Sequence stratigraphy of Comanchean Cretaceous outcrop strata of northeast and south-central Texas: Implications for enhanced petroleum exploration: *Gulf Coast Association of Geological Societies Transactions*, v. 56, p. 539-550.

Martens, U., Weber, B., Valencia, V.A., 2010. U/Pb geochronology of Devonian and older Paleozoic beds in the southeastern Maya block, Central America: Its affinity with peri-Gondwanan terranes: *Bulletin of the Geological Society of America*, v. 122, p. 815-829.

Martini, M., Ortega- Gutiérrez, 2016. Tectono-stratigraphic evolution of eastern Mexico during the break-up of Pangea: A review: *Earth-Science Review*

Maxwell, R. A. and J. W. Dietrich, 1972. Geology of the Big Bend area, Texas: *West Texas Geological Society, Midland, Texas*, v. 65, p. 248.

McLennan, S.M., Bock, B., Compston, W., Hemming, S.R., McDaniel, D.K., 2001. Detrital zircon geochronology of Taconian and Acadian foreland sedimentary rocks in New England: *Journal of Sedimentary Research*, v. 71, p. 305-317.

McMillan, N.J., and McLemore, V.T., 2004. Cambro-Ordovician magmatism andextension in New Mexico and Colorado: *New Mexico Bureau of Geology and Mineral Resources, Bulletin*, v. 160, p. 1–11.

Michalzik, D., 1991. Facies sequence of Triassic–Jurassic red beds in the Sierra Madre Oriental (NE Mexico) and its relation to the early opening of the Gulf of Mexico: *Sediment. Geol*., v. 71, p. 243–259.

Miller, C.F., Hatcher R.D., Jr., Ayers, J.C., Coath, C.D., Aand Harrison, T.M., 2000. Age and zircon inheritance of eastern Blue Ridge plutons, southwestern North Carolina and northeastern Georgia, with implications for magma history and evolution of the southern Appalachian orogen: *American Journal of Science*, v. 300, p. 142–172.

Moecher, D., Samson, S., 2006. Differential zircon fertility of source terranes and natural bias in the detrital zircon record: Implications for sedimentary provenance analysis: *Earth and Planetary Science Letters*, v. 247, p. 252-266.

Moecher, D., Hietpas, J., Samson, S., Chakraborty, S., 2011. Insights into southern Appalachian tectonics from ages of detrital monazite and zircon in modern alluviam: *Geosphere*, v.7, no. 2, p. 494-512.

Mueller, P.A., Heatherington, A.L., Wooden, J.L., Shuster, R.D., Nutman, A.P., Williams, I.S., 1994. Precambrian zircons from the Florida basement; a Gondwanan connection: *Geology (Boulder)*, v. 22, p. 119-122.

Mullens, H.T., et al., 1980. Nodular Carbonate Sediment on Bahamian Slopes: Possible Precursors to Nodular Limestones: *Journal of Sedimentary Petrology*, v. 50, p. 117-131.

Murphy, J.B., Pisarevsky, S.A., Nance, R.D., Keppie, J.D., 2004. Neoproterozoic-early Paleozoic evolution of peri-Gondwanan terranes; implications for Laurentia- Gondwana connections: *International Journal of Earth Sciences*, v. 93, p. 659-682.

Myrow, P. M., W. Fischer, and J. W. Goodge, 2002. Wave-modified turbidites; combined-flow shoreline and shelf deposits, Cambrian, Central Transantarctic Mountains: *Journal of Sedimentary Research*, v. 72, p. 641-656.

Ogg, J.G., and Hinnov, L.A., 2012. Cretaceous. In: The Geologic Time Scale 2012 (Gradstein, F.M., Ogg, J.G., Schmitz, M.D., and Ogg, G.M., editors): *Elsevier Publ*

Park, H., Barbeau, D.L., Jr., Rickenbaker, A., Bachmann-Krug, D., Gehrels, G.E., 2010. Application of foreland basin detrital-zircon geochronology to the reconstruction of the Southern and Central Appalachian Orogen: *Journal of Geology*, v. 118, p. 23-44.

Phelps, R. M., et al., 2014. Oceanographic and Eustatic Control of Carbonate Platform Evolution and Sequence Stratigraphy on the Cretaceous (Valanginian-Campanian) Passive Margin, Northern Gulf of Mexico: *Sedimentology*, v. 61, p. 461-496.

Rose, Peter R., 1974. Edwards Group, Surface and Subsurface, Central Texas: *Houston Geological Society Bulletin*, v. 17, p. 3.

Schlanger, S. O. and H. C. Jenkyns, 1976. Cretaceous oceanic anoxic events Causes and consequences: *Geologie en Mijnbouw*, v. 55, p. 179-184.

Scott, R.J., 2004. The Maverick Basin: New Technology- New Success: *Gulf Coast Association of Geological Societies Transactions*: v. 54, p. 603-620.

Sláma, J., Košler, J., Condon, D. J., Crowley, J. L., Gerdes, A., Hanchar, J. M., & Whitehouse, M. J., 2008. Plešovice zircon—a new natural reference material for U–Pb and Hf isotopic microanalysis: *Chemical Geology*, v. 249, p. 1-35.

Stewart, J.H., Blodgett, R.B., Boucot, A.J., Carter, J.L., Lopez, R., 1999. Exotic Paleozoic strata of Gondwanan provenance near Ciudad Victoria, Tamaulipas, Mexico: *Geological Society of America*, v. 336, p. 227-252.

Soreghan, G.S., Soreghan, M.J., 2013. Tracing clastic delivery to the Permian Delaware Basin, U.S.A.; implications for paleogeography and circulation in westernmost equatorial Pangea: *Journal of Sedimentary Research*, v. 83, p. 786-802.

Su, Q., Goldberg, S.A., and Fullager, P.D., 1994. Precise U-Pb zircon ages of Neoproterozoic plutons in the southern Appalachian Blue Ridge and their implications for the initial rifting of Laurentia: *Precambrian Research*, v. 68, p. 81–95

Thomas, W.A., Becker, T.P., Samson, S.D., Hamilton, M.A., 2004. Detrital zircon evidence of a recycled orogenic foreland provenance for Alleghanian clasticwedge sandstones: *Journal of Geology*, v. 112, p. 23-37.

Thomas, W.A., 2011. Detrital Zircon Geochronology and Sedimentary Provenance: *Geological Society of America*, v. 3, p. 304-308.

Vega-Granillo, Ricard, et al., 2008. U–Pb detrital zircon data of the Rio Fuerte Formation (NW Mexico): Its peri-Gondwanan provenance and exotic nature in relation to southwestern North America: *Journal of South American Earth Sciences*, v. 26, p. 343-354.

Van Wagoner, J.C., Mitchum Jr., R.M., Campion, K.M., Rahmanian, V.D., 1990. Siliciclastic sequence stratigraphy in well logs, core, and outcrops: concepts for high-resolution correlation of time and facies: *American Association of Petroleum Geologists Methods in Exploration Series*, v. 7, p. 55.

Walker, N., 1992. Middle Proterozoic Geologic Evolution of Llano Uplift, Texas: Evidence from U-Pb Zircon Geochronometry: *Geological Society of America*, v. 104, p. 494-504.

Weber, B., Schaaf, P., Valencia, V.A., Iriondo, A., Ortega-Gutierrez, F., 2006. Provenance ages of late Paleozoic sandstones (Santa Rosa Formation) from the Maya Block, SE Mexico; implications on the tectonic evolution of western Pangea: *Revista Mexicana de Ciencias Geologicas*, v. 23, p. 262-276.

Weissert, H., A. Lini, K. B. Föllmi, and O. Kuhn, 1998. Correlation of Early Cretaceous carbon isotope stratigraphy and platform drowning events: A possible link?: *Palaeogeogr. Palaeoclimatol. Palaeoecol.*, v. 137, p. 189–203.

Yang, B. C., R. W. Dalrymple, and S. S. Chun, 2005. Sedimentation on a wave-dominated, open-coast tidal flat, south- western Korea; summer tidal flat-winter shoreface: *Sedimentology*, v. 52, p. 235-252.

Yonkee, A.W., Weil, A.B., 2015. Tectonic evolution of the Seveir and Laramide belts within the North American Cordillera orogenic system: *Earth-Science Review*, v. 150, p. 531-593.

APPENDIX A

	Outcroup Name	Latitude	Longitude	Location Description
1	East Comstock	29.67764ºN	101.15842 ºW	East of Comstock, off Highway 90
2	Comstock Town	29.68588 ºN	101.17100 ºW	In the town of Comstock of Highway 90
3	West Comstock	29.69525 ºN	101.18780 ºW	West of Comstock, off Highway 90
4	Seminole Canyon	29.70651 ºN	101.31570 ºW	Across entrance of Seminole Canyon State Park, off Highway 90
5	East Pecos River	29.70429 ºN	101.34695 ºW	East side of the Pecos River Canyon Bridge, off of Highway 90
6	West Pecos River	29.74481 ºN	101.38611 ºW	West side of Pecos River about 3 miles, off of Highway 90
7	Prairie Creek	29.99530 ºN	102.02934 ºW	Off of Highway 90, about 5 miles east of Dryden, near Prairie Creek
8	Dryden West	30.05114 ºN	102.15511 ºW	3 miles west of Dryden, off of Highway 90
9	Dagger Flats	29.50338 ºN	103.05315 ºW	Off of Dagger Flats road in Big Bend National Park
10	Hot Springs	29.18591 ºN	102.98426 ºW	Off of the Hot Springs Historic Trail in Big Bend National Park
11	West Terlingua	29.31712 ºN	103.65817 ºW	About 3.5 miles West of Terlingua, along Highway 170, near Villa Delamina Rd.

Table A-1. Latitude and longitude of outcrops as well as general location descriptions.

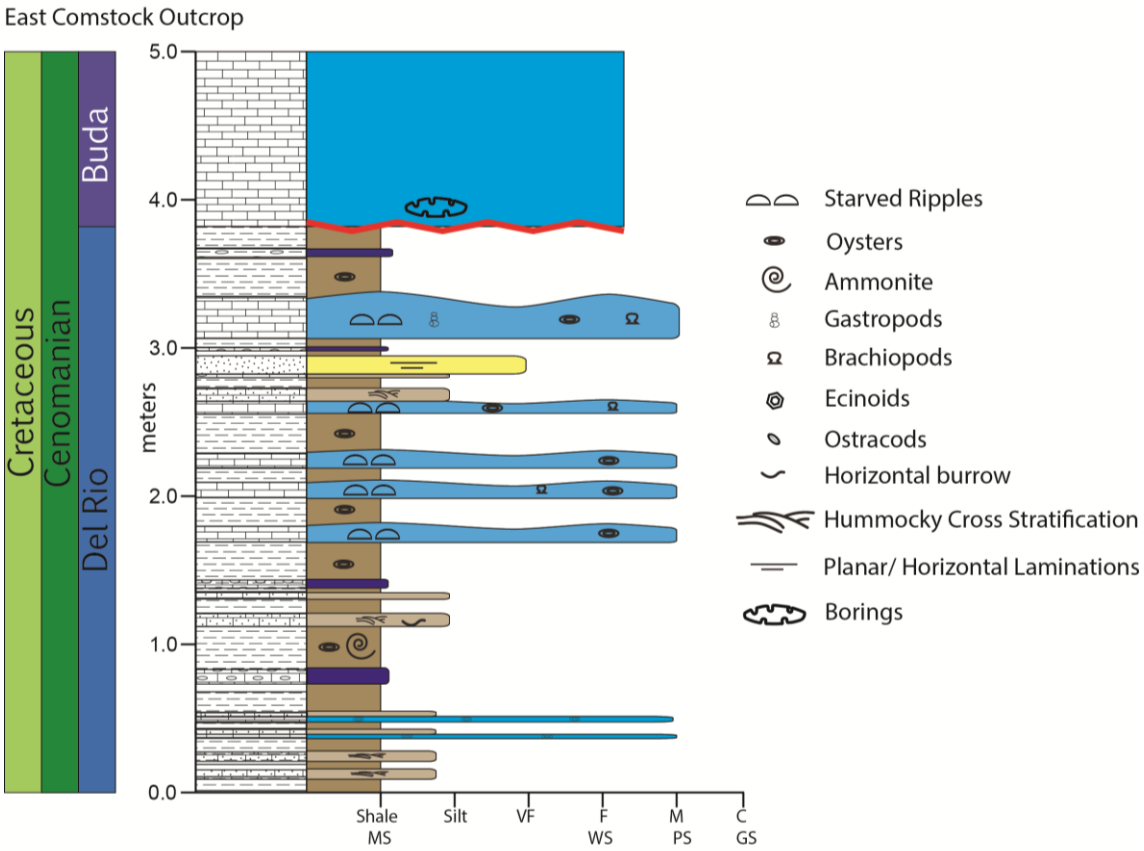

Figure A-1. Measured section of East Comstock outcrop.

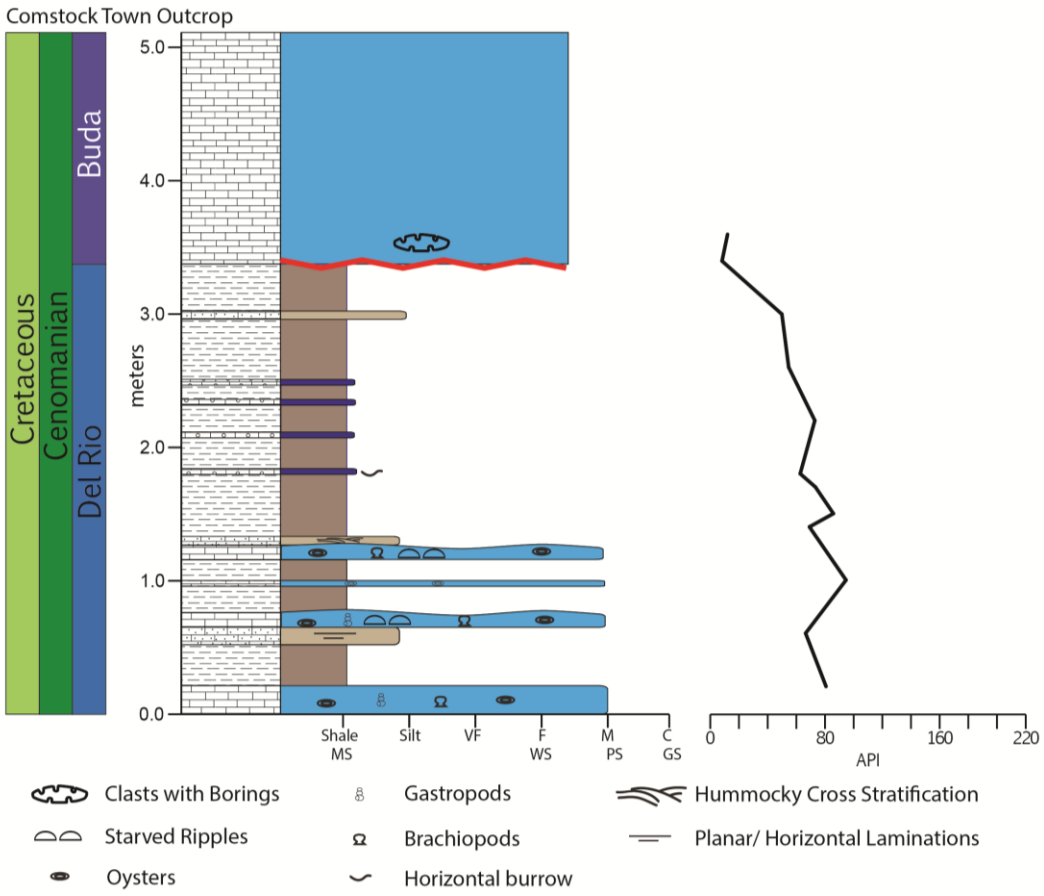

Figure A-2. Measured section of the Comstock Town outcrop.

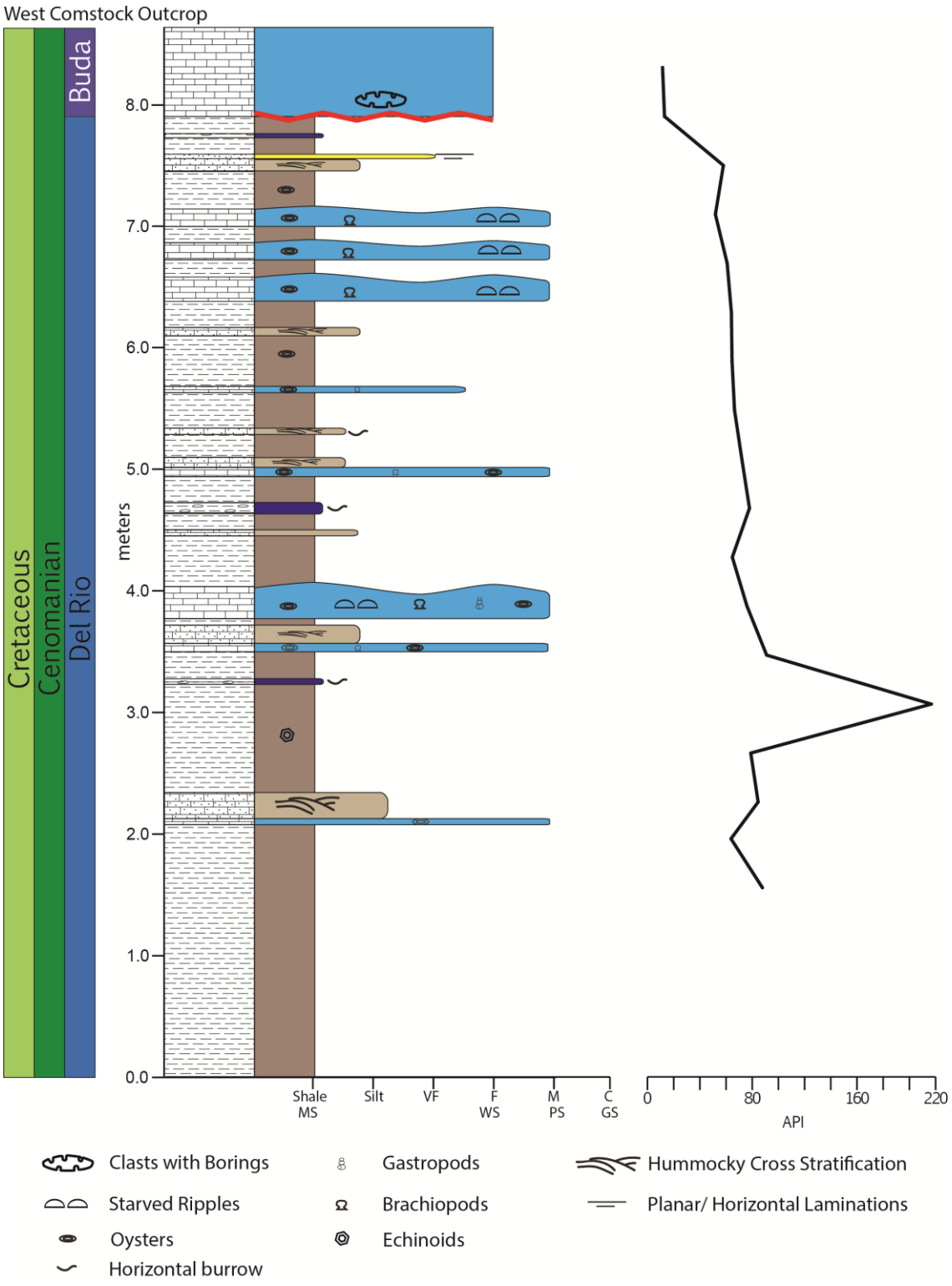

Figure A-3. Measured section of the West Comstock outcrop.

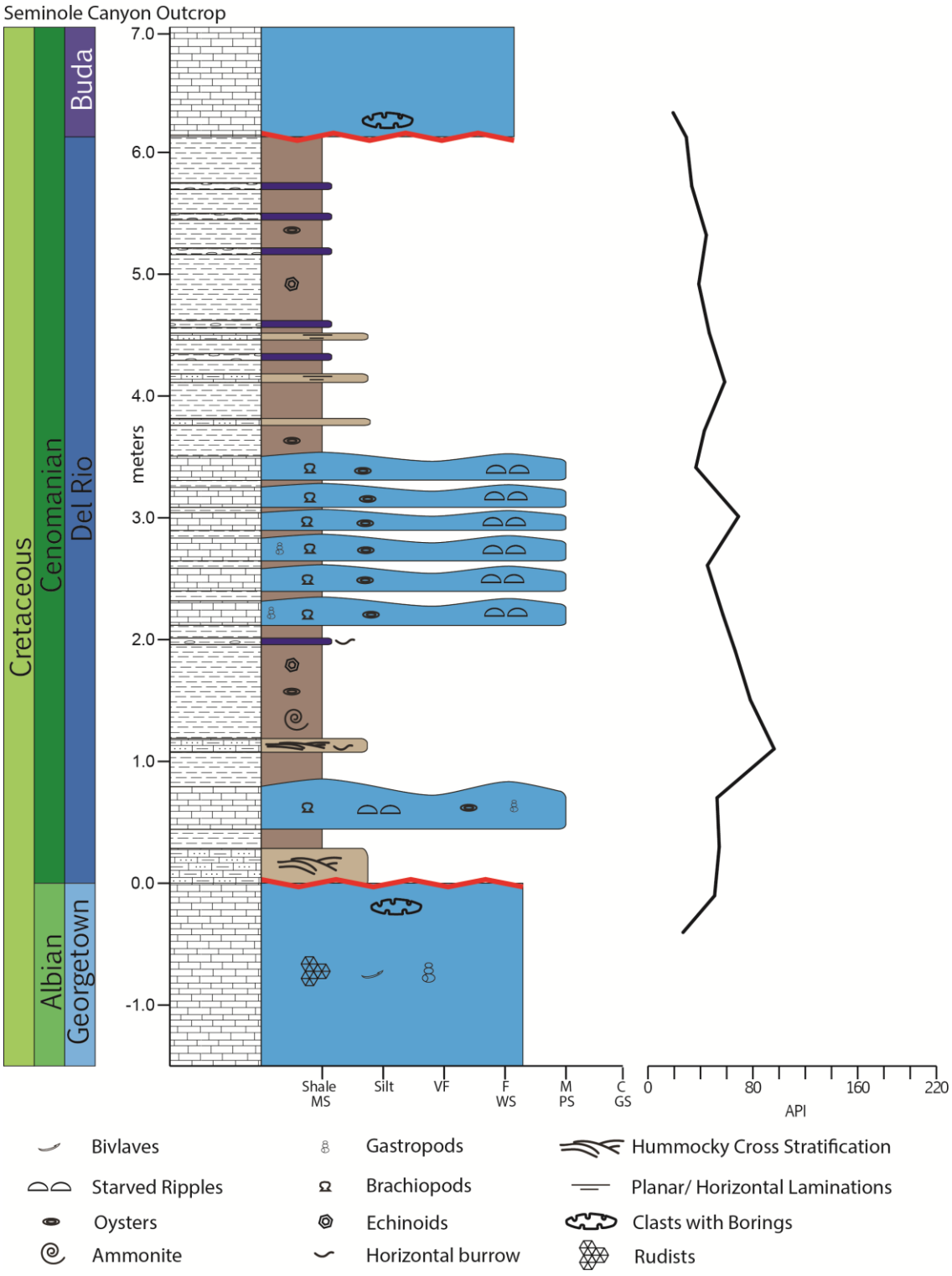

Figure A-4. Measured section of the Seminole Canyon outcrop.

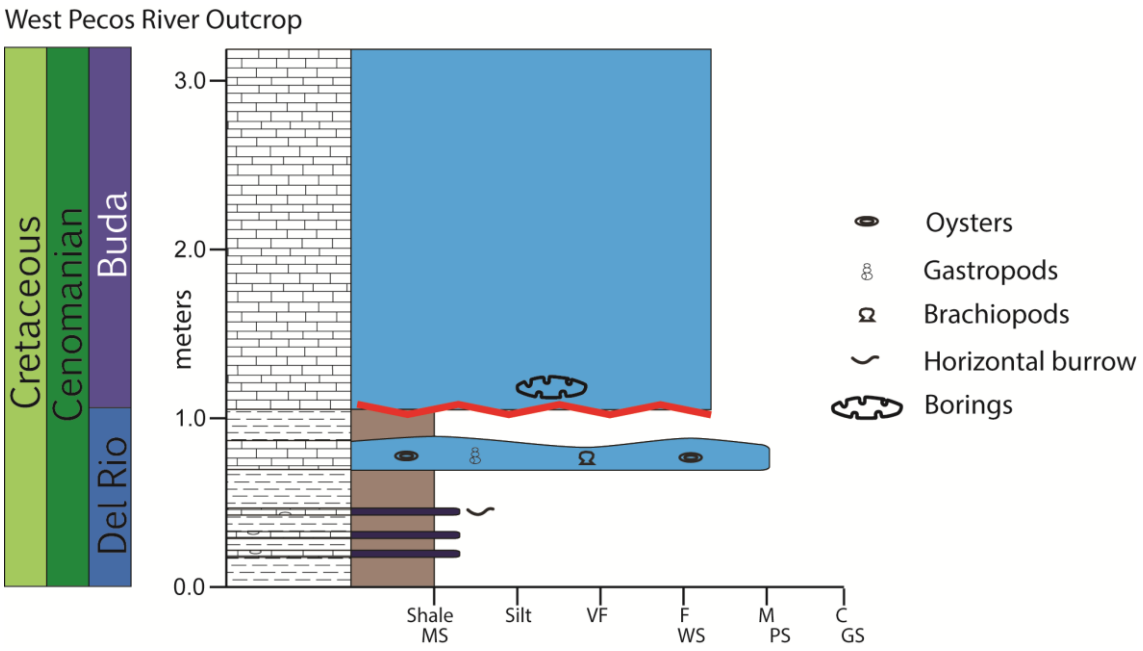

Figure A-5. Measured section of the West Pecos River Outcrop.

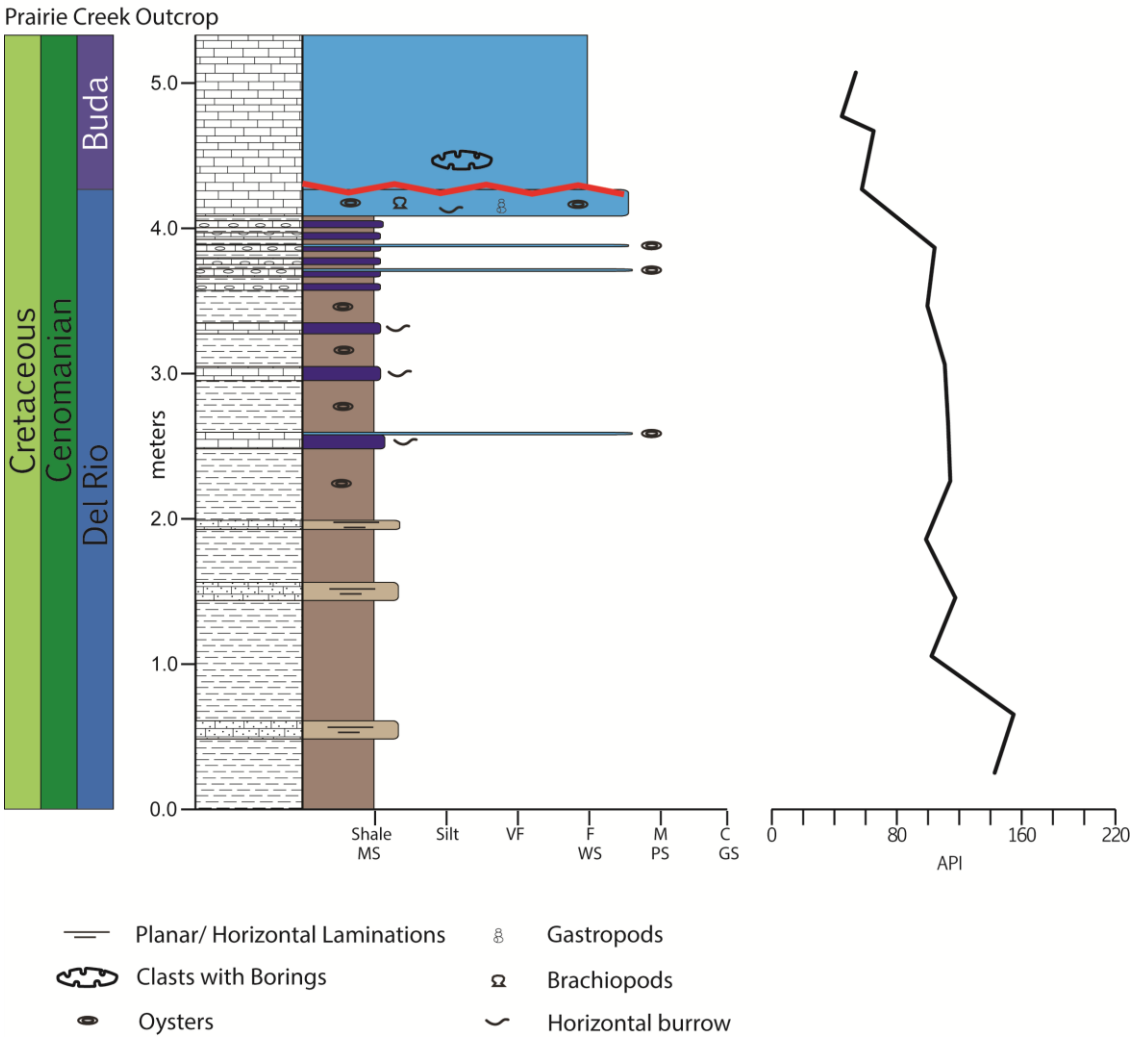

Figure A-6. Measured section of the Prairie Creek outcrop.

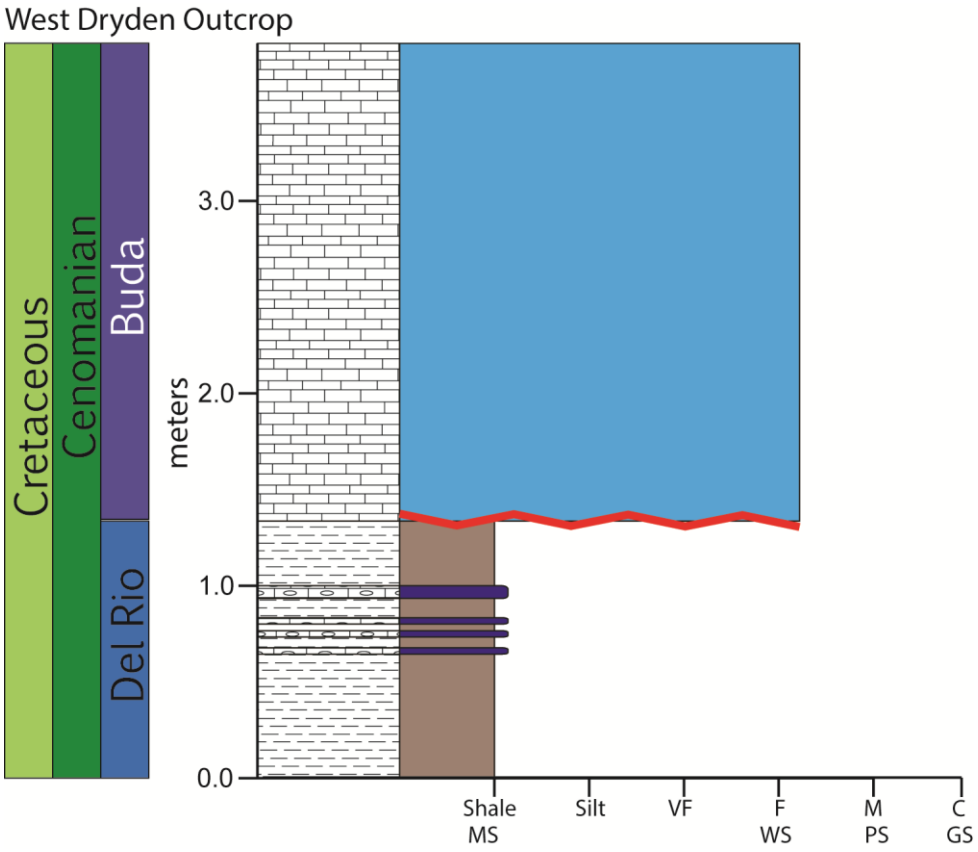

Figure A-7. Measured section of the West Dryden outcrop.

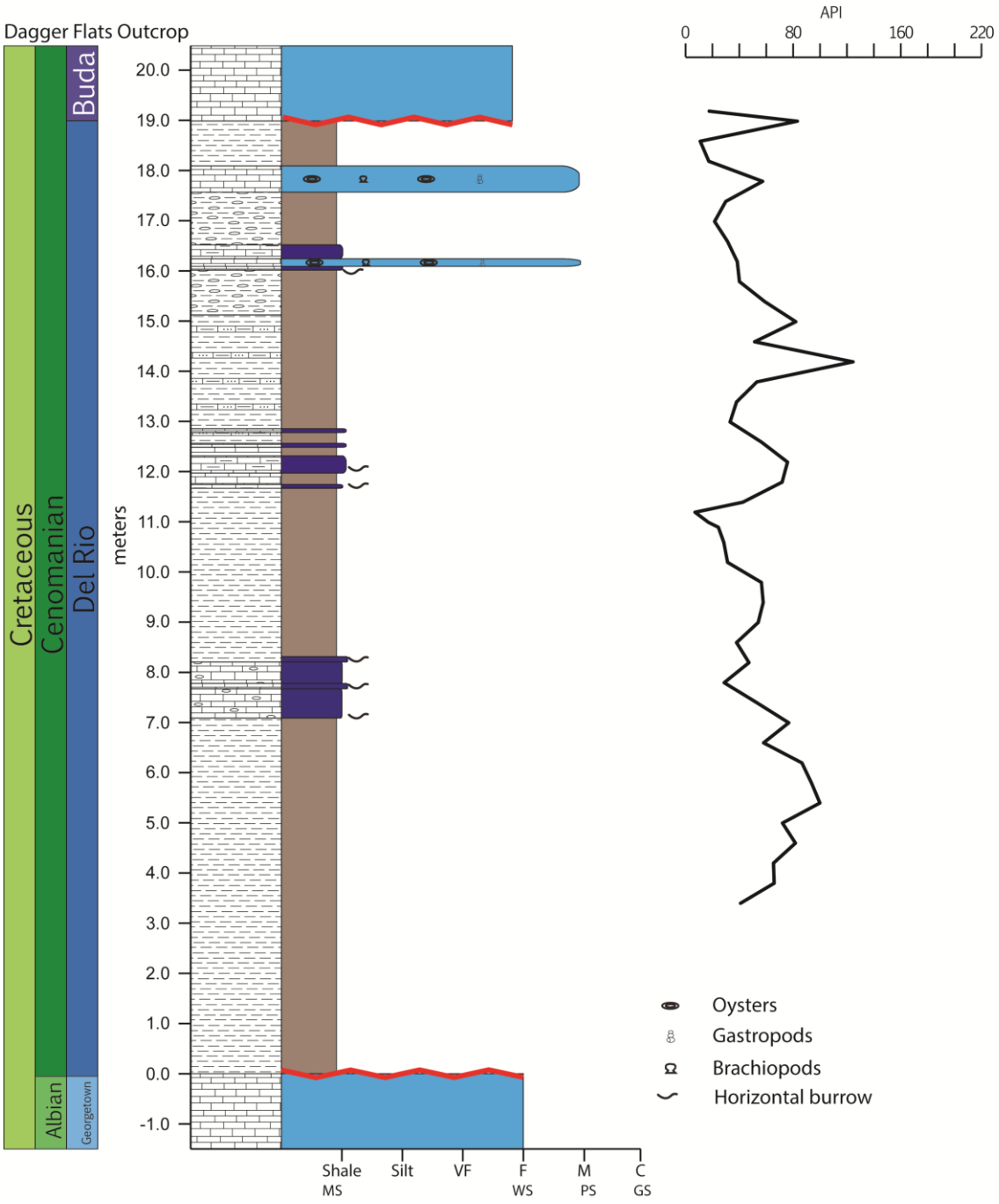

Figure A-8. Measured section of the Dagger Flats outcrop.

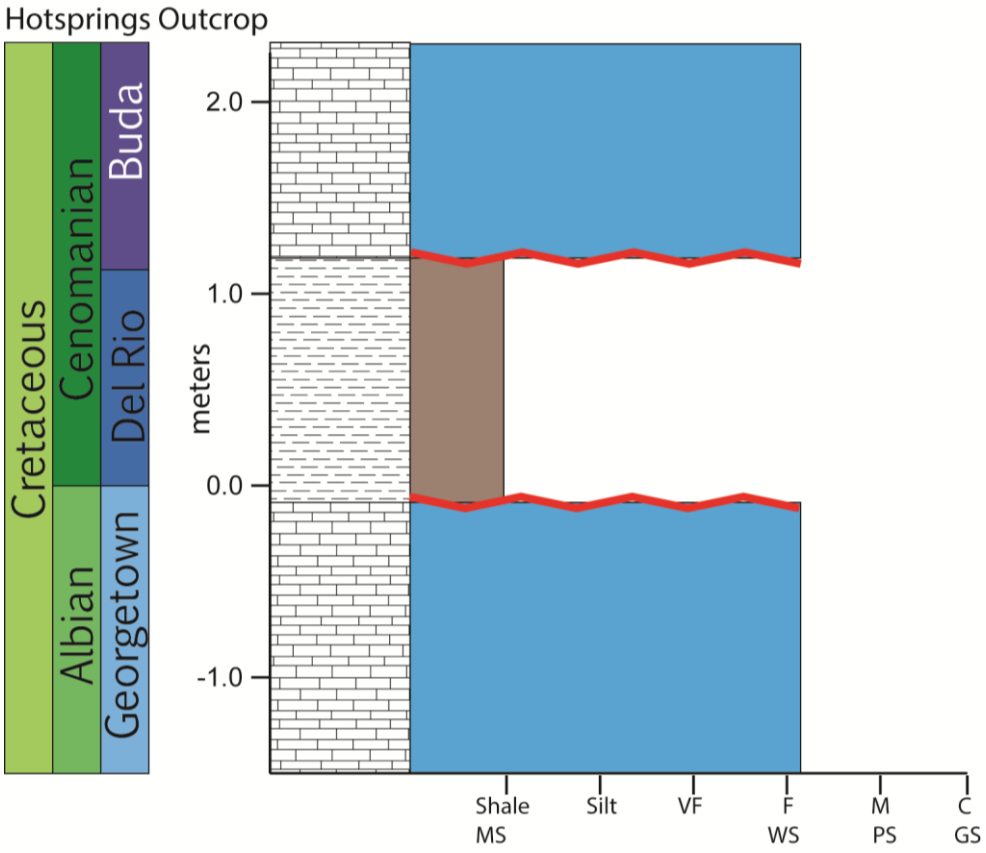

Figure A-9. Measured section of the Hotsprings outcrop.

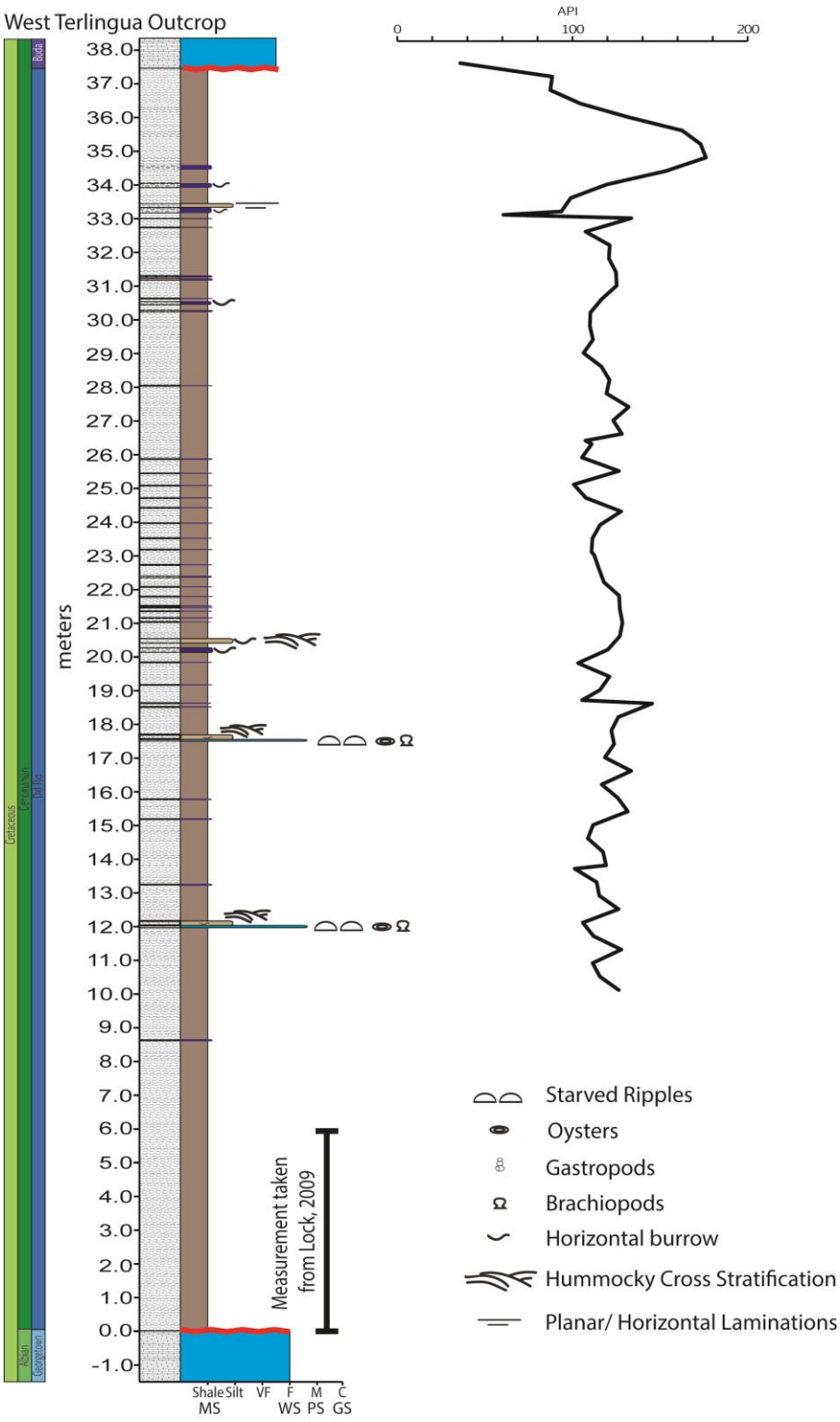

Figure A-10. Measured section of the West Terlingua outcrop.

APPENDIX B

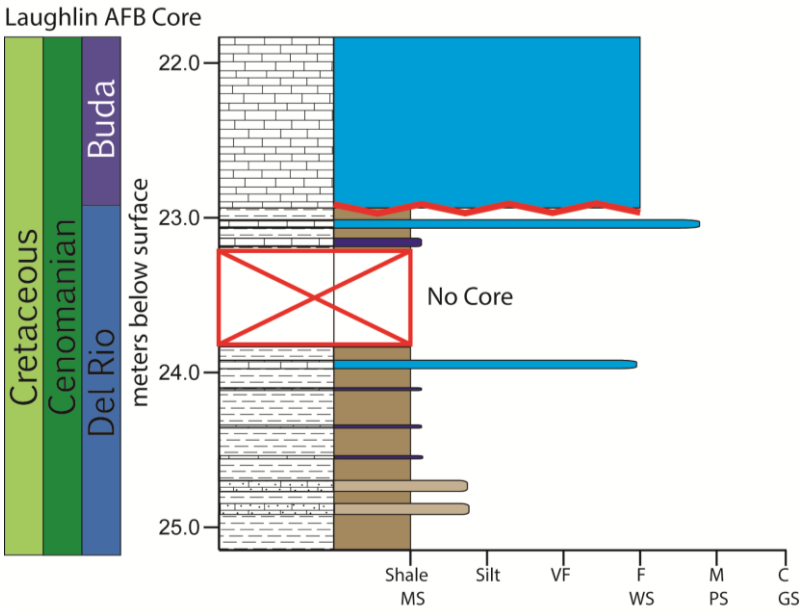

Figure B-1. Laughlin AFB core measured section.

Figure B-2. Photo of whole Laughlin AFB core. Showing contact of the white colored Buda Formation with the dark grey Del Rio Formation

APPENDIX C

Table C-1. Isotopic ratios and Apparent Ages for sample EC1b. Discordance < 20%.

	Isotopic Ratios						Ap. Age							
Sample Name	$^{207}Pb/^{206}Pb$	1σ abs.	$^{207}Pb/^{235}U$	1σ abs.	$^{206}Pb/^{238}U$	1σ abs.	$^{207}Pb/^{206}Pb$	1σ abs.	$^{207}Pb/^{235}U$	1σ abs.	$^{206}Pb/^{238}U$	1σ abs.	Best Age	Best Age Error
EC1b-01	0.074	6.145	1.749	8.467	0.172	5.859	1036.64	124.1	1026.83	54.75	1021.51	55.35	1021.5	55.35
EC1b-02	0.172	5.819	11.463	8.298	0.482	5.950	2578.94	97.18	2561.55	77.65	2538.04	124.84	2578.9	97.18
EC1b-03	0.046	8.150	0.099	10.75	0.016	7.052	0.00	196.4	95.58	9.82	99.99	7.00	99.99	7.00
EC1b-04	0.053	10.119	0.114	12.11	0.016	6.697	319.69	229.9	110.02	12.64	100.50	6.68	100.50	6.68
EC1b-05	0.106	8.011	4.332	11.36	0.297	8.089	1728.12	147.0	1699.50	94.05	1675.28	119.35	1728.1	147.07
EC1b-06	0.056	6.458	0.210	8.920	0.027	6.183	434.52	143.8	193.50	15.72	174.18	10.63	174.18	10.63
EC1b-07	0.084	7.052	2.423	9.636	0.210	6.595	1285.35	137.3	1249.43	69.36	1227.86	73.74	1285.3	137.33
EC1b-09	0.075	5.986	1.895	8.042	0.183	5.405	1066.62	120.3	1079.33	53.50	1084.90	53.97	1084.9	53.97
EC1b-10	0.091	6.060	3.196	8.300	0.254	5.704	1451.34	115.3	1456.31	64.28	1458.77	74.46	1451.3	115.33
EC1b-12	0.049	7.709	0.102	10.36	0.015	6.950	133.68	181.2	98.43	9.72	96.91	6.69	96.91	6.69
EC1b-13	0.064	10.854	0.728	13.31	0.083	7.734	735.50	229.7	555.13	57.00	511.80	38.05	511.80	38.05
EC1b-14	0.080	5.955	2.073	8.198	0.189	5.666	1185.52	117.6	1139.80	56.21	1115.19	58.03	1115.1	58.03
EC1b-15	0.047	9.946	0.106	12.26	0.016	7.193	52.01	237.4	102.00	11.90	104.07	7.43	104.07	7.43
EC1b-17	0.162	6.033	9.407	8.544	0.422	6.079	2472.84	101.8	2378.47	78.57	2268.53	116.27	2472.8	101.82
EC1b-19	0.078	7.892	2.090	11.11	0.194	7.843	1145.90	156.8	1145.53	76.45	1144.58	82.25	1144.5	82.25
EC1b-20	0.097	7.381	3.208	11.63	0.239	9.017	1570.45	138.2	1459.09	90.32	1382.93	112.24	1570.4	138.28
EC1b-21	0.056	7.517	0.495	9.512	0.064	5.857	463.36	166.5	408.17	31.98	398.20	22.62	398.20	22.62
EC1b-22	0.082	7.659	2.405	10.76	0.213	7.584	1240.48	150.1	1244.10	77.33	1245.39	85.89	1240.4	150.10
EC1b-23	0.077	7.434	2.035	10.55	0.191	7.510	1125.63	148.1	1127.20	71.95	1127.28	77.67	1127.2	77.67
EC1b-24	0.073	9.404	1.790	13.15	0.177	9.221	1025.08	190.2	1041.78	85.91	1049.08	89.28	1049.0	89.28
EC1b-25	0.056	9.673	0.545	13.32	0.070	9.187	462.21	214.3	441.85	47.78	437.65	38.87	437.65	38.87
EC1b-26	0.060	9.882	0.438	13.65	0.053	9.443	602.27	213.8	368.67	42.24	332.36	30.59	332.36	30.59
EC1b-27	0.100	7.985	3.879	11.39	0.281	8.157	1627.57	148.4	1609.33	92.28	1594.44	115.23	1627.5	148.49
EC1b-28	0.061	10.617	0.796	14.83	0.094	10.377	656.28	227.7	594.53	66.85	578.09	57.38	578.09	57.38
EC1b-29	0.079	6.344	2.178	8.885	0.201	6.247	1161.71	125.7	1174.11	61.90	1180.09	67.37	1180.0	67.37
EC1b-30	0.097	6.431	3.448	8.838	0.257	6.091	1571.79	120.4	1515.33	69.67	1474.31	80.27	1571.7	120.45
EC1b-32	0.082	6.795	2.307	9.746	0.205	7.011	1237.41	133.2	1214.50	69.14	1200.88	76.82	1237.4	133.22
EC1b-33	0.056	9.572	0.458	13.29	0.060	9.249	443.29	212.8	383.01	42.45	372.85	33.51	372.85	33.51
EC1b-34	0.081	6.284	2.132	8.673	0.191	6.006	1223.79	123.4	1159.20	60.01	1124.22	61.97	1124.2	61.97
EC1b-35	0.063	6.783	0.853	9.320	0.099	6.418	694.82	144.5	626.20	43.58	606.95	37.18	606.95	37.18
EC1b-36	0.079	10.020	1.224	16.45	0.113	13.063	1160.36	198.6	811.54	92.19	689.85	85.46	689.85	85.46
EC1b-37	0.078	9.446	1.079	13.54	0.100	9.722	1144.32	187.7	743.22	71.49	616.75	57.18	616.75	57.18
EC1b-38	0.080	7.488	2.073	10.56	0.189	7.474	1188.67	147.8	1139.98	72.48	1113.84	76.46	1113.8	76.46
EC1b-39	0.064	10.839	0.825	14.40	0.094	9.501	731.07	229.6	610.73	66.19	578.38	52.56	578.38	52.56
EC1b-40	0.073	10.864	1.706	15.42	0.170	10.965	1003.73	220.5	1010.89	99.06	1013.51	102.84	1013.5	102.84
EC1b-42	0.048	10.386	0.102	12.18	0.016	6.397	77.84	246.7	99.04	11.50	99.84	6.34	99.84	6.34
EC1b-43	0.103	8.624	4.136	12.13	0.291	8.554	1681.76	159.2	1661.51	99.52	1644.44	124.17	1681.7	159.25
EC1b-44	0.076	7.541	1.699	11.02	0.162	8.066	1100.88	150.8	1008.20	70.59	965.41	72.32	965.41	72.32
EC1b-45	0.090	6.093	2.942	8.580	0.238	6.071	1416.23	116.5	1392.67	65.11	1376.38	75.25	1416.2	116.51
EC1b-47	0.082	8.695	1.312	13.90	0.116	10.863	1238.46	170.4	850.93	80.26	709.54	72.99	709.54	72.99
EC1b-48	0.111	11.059	4.585	16.17	0.299	11.819	1814.98	200.8	1746.54	135.6	1688.76	175.64	1814.9	200.85
EC1b-49	0.124	6.017	5.549	8.759	0.325	6.394	2009.17	106.7	1908.25	75.50	1815.53	101.18	2009.1	106.78
EC1b-50	0.075	6.416	1.692	8.682	0.163	5.880	1072.10	128.8	1005.64	55.46	974.67	53.19	974.67	53.19
EC1b-51	0.073	15.246	1.652	21.64	0.163	15.374	1027.29	308.4	990.47	137.7	973.18	138.89	973.18	138.89

Table C-1 Continued

EC1b-52	0.09	8.488	3.28	11.379	0.253	7.603	1508.78	160.3	1478.02	88.82	1455.5	99.07	1508.7	160.31
EC1b-53	0.06	6.605	0.70	9.757	0.082	7.207	689.45	140.8	540.62	40.92	505.57	35.04	505.57	35.04
EC1b-54	0.08	5.867	2.05	8.144	0.184	5.681	1223.94	115.2	1135.32	55.72	1088.6	56.91	1088.6	56.91
EC1b-55	0.08	9.647	2.56	13.714	0.218	9.767	1315.95	187.0	1289.28	100.46	1272.3	112.78	1315.9	187.05
EC1b-56	0.11	5.779	4.75	8.500	0.310	6.263	1819.26	104.9	1776.38	71.42	1738.7	95.46	1819.2	104.90
EC1b-57	0.08	7.783	2.04	10.449	0.186	6.999	1189.49	153.6	1130.16	71.36	1098.6	70.70	1098.6	70.70
EC1b-58	0.05	7.048	0.45	9.730	0.056	6.736	565.25	153.4	380.49	30.89	350.51	22.98	350.51	22.98
EC1b-59	0.09	6.654	3.58	9.489	0.262	6.793	1604.39	124.1	1546.04	75.47	1502.4	91.05	1604.3	124.12
EC1b-60	0.08	6.310	2.18	8.766	0.185	6.116	1331.13	122.0	1176.69	61.15	1093.5	61.52	1093.5	61.52
EC1b-61	0.05	9.133	0.18	11.625	0.027	7.219	187.07	212.5	172.99	18.49	171.80	12.24	171.80	12.24
EC1b-62	0.06	6.864	0.83	9.178	0.096	6.124	714.92	145.8	617.33	42.48	590.49	34.56	590.49	34.56
EC1b-63	0.07	12.57	1.24	14.618	0.118	7.478	1105.80	251.3	822.65	82.59	721.18	51.02	721.18	51.02
EC1b-64	0.07	5.843	1.99	8.109	0.189	5.658	1105.72	116.7	1112.84	54.88	1115.4	57.96	1115.4	57.96
EC1b-65	0.10	7.791	3.60	10.840	0.254	7.564	1673.66	144.0	1550.88	86.38	1460.9	98.89	1673.6	144.00
EC1b-67	0.08	6.218	2.53	8.830	0.211	6.301	1355.96	119.8	1281.68	64.37	1236.6	70.90	1355.9	119.88
EC1b-69	0.07	6.197	1.73	8.693	0.171	6.129	1028.28	125.3	1020.68	56.02	1016.1	57.62	1016.1	57.62
EC1b-70	0.06	10.63	0.92	14.717	0.101	10.19	800.02	222.8	662.47	71.73	622.11	60.45	622.11	60.45
EC1b-71	0.05	10.39	0.54	14.252	0.069	9.771	501.41	228.8	443.65	51.27	432.11	40.84	432.11	40.84
EC1b-72	0.08	6.785	2.87	9.843	0.236	7.158	1382.19	130.3	1374.49	74.26	1368.1	88.24	1382.1	130.34
EC1b-73	0.07	6.651	1.97	9.328	0.186	6.571	1122.04	132.6	1108.41	63.00	1100.2	66.47	1100.2	66.47
EC1b-74	0.08	6.987	2.05	10.047	0.187	7.247	1184.92	138.0	1134.82	68.76	1107.5	73.76	1107.5	73.76
EC1b-76	0.11	5.796	4.53	7.964	0.282	5.498	1900.03	104.1	1736.44	66.34	1602.1	78.00	1900.0	104.17
EC1b-77	0.07	7.263	1.60	9.595	0.157	6.300	1039.25	146.6	970.24	60.02	938.98		938.98	55.05
EC1b-78	0.08	6.366	2.35	9.771	0.205	7.439	1274.97	124.1	1228.18	69.72	1200.3	81.47	1274.9	124.15
EC1b-79	0.08	5.823	2.57	8.031	0.214	5.565	1367.45	112.1	1293.95	58.81	1248.6	63.18	1367.4	112.10
EC1b-80	0.08	10.49	3.11	14.921	0.253	10.62	1411.43	200.8	1436.49	115.18	1451.8	138.12	1411.4	200.84
EC1b-81	0.08	10.74	2.88	15.547	0.241	11.25	1353.38	207.1	1376.66	117.70	1390.1	140.80	1353.3	207.15
EC1b-82	0.10	6.441	3.43	9.002	0.241	6.320	1679.87	118.9	1511.91	70.90	1393.2	79.20	1679.8	118.96
EC1b-83	0.08	8.255	1.82	11.520	0.165	8.059	1198.79	162.7	1055.82	75.76	986.82	73.74	986.82	73.74
EC1b-84	0.08	6.951	2.53	9.744	0.210	6.857	1374.71	133.6	1283.41	71.10	1228.0	76.68	1374.7	133.67
EC1b-86	0.06	6.972	1.31	9.701	0.137	6.774	906.52	143.6	851.40	55.97	829.37	52.72	829.37	52.72
EC1b-87	0.05	10.76	0.10	14.683	0.016	10.00	192.54	250.2	104.18	14.54	100.23	9.95	100.23	9.95
EC1b-88	0.07	8.571	1.82	12.554	0.172	9.194	1115.92	171.0	1054.74	82.54	1024.1	87.07	1024.1	87.07
EC1b-89	0.08	5.557	2.31	7.817	0.202	5.532	1264.78	108.5	1216.52	55.47	1188.0	60.02	1188.0	60.02
EC1b-90	0.07	6.235	1.70	8.728	0.171	6.138	998.37	126.6	1012.06	55.97	1017.1	57.76	1017.1	57.76
EC1b-91	0.05	9.416	0.11	12.464	0.017	8.190	184.18	219.3	113.69	13.41	110.20	8.95	110.20	8.95
EC1b-92	0.08	6.908	1.49	9.331	0.122	6.303	1405.50	132.2	928.48	56.84	739.80	44.05	739.80	44.05
EC1b-93	0.07	6.620	1.69	9.244	0.165	6.481	1048.34	133.4	1006.82	59.10	986.62	59.29	986.62	59.29
EC1b-94	0.07	6.161	0.56	10.424	0.056	8.432	1021.89	124.7	453.62	38.15	349.20	28.66	349.20	28.66
EC1b-95	0.08	11.19	2.41	14.951	0.203	9.935	1345.84	216.0	1246.86	107.75	1188.8	107.88	1188.8	107.88
EC1b-96	0.05	6.978	0.71	9.471	0.090	6.433	517.99	153.1	549.82	40.23	556.83	34.32	556.83	34.32
EC1b-97	0.05	6.306	0.39	8.902	0.049	6.313	564.26	137.3	340.43	25.75	308.15	18.99	308.15	18.99
EC1b-98	0.06	6.186	0.55	8.331	0.067	5.613	592.73	134.0	445.09	30.03	416.53	22.64	416.53	22.64
EC1b-99	0.12	7.598	6.36	11.337	0.359	8.437	2078.05	133.7	2027.90	99.81	1976.7	143.65	2078.0	133.76
EC1b-100	0.05	11.47	0.12	13.541	0.016	7.211	425.20	255.9	115.37	14.77	100.77	7.21	100.77	7.21
EC1b-101	0.06	7.196	0.47	9.388	0.053	6.060	738.84	152.2	392.28	30.56	335.63	19.82	335.63	19.82
EC1b-103	0.08	6.005	2.70	8.204	0.228	5.623	1338.98	116.0	1330.17	60.90	1323.2	67.27	1338.9	116.06

Table C-1 Continued

EC1b-104	0.09	9.046	3.156	12.976	0.253	9.323	1435.74	172.5	1446.36	100.38	1452.0	121.22	1435.7	172.53
EC1b-105	0.08	6.047	2.163	8.703	0.194	6.289	1211.72	119.0	1169.21	60.50	1145.1	65.99	1145.1	65.99
EC1b-106	0.05	7.811	0.431	10.381	0.057	6.865	400.03	175.0	364.10	31.77	358.09	23.91	358.09	23.91
EC1b-107	0.05	9.815	0.630	13.605	0.080	9.440	502.61	216.0	496.29	53.46	494.40	44.93	494.40	44.93
EC1b-108	0.07	6.441	1.741	8.932	0.173	6.218	1006.50	130.6	1023.94	57.67	1031.1	59.25	1031.1	59.25
EC1b-109	0.05	7.321	0.591	9.413	0.074	5.948	532.67	160.3	471.38	35.51	458.43	26.32	458.43	26.32
EC1b-110	0.08	5.907	2.193	8.230	0.192	5.763	1258.59	115.4	1178.76	57.45	1134.6	59.96	1134.6	59.96
EC1b-111	0.06	7.501	0.774	10.807	0.091	7.803	652.34	160.9	582.12	47.92	563.77	42.13	563.77	42.13
EC1b-112	0.05	11.58	0.555	15.815	0.071	10.78	482.70	255.8	448.43	57.39	441.40	46.00	441.40	46.00
EC1b-113	0.05	17.92	0.150	21.808	0.020	12.44	429.80	399.4	141.62	28.83	124.91	15.39	124.91	15.39
EC1b-114	0.07	9.990	2.108	14.729	0.200	10.84	1109.44	199.5	1151.52	101.78	1173.1	116.29	1173.1	116.29
EC1b-115	0.07	10.36	1.727	14.755	0.169	10.51	1044.29	209.1	1018.45	95.15	1005.7	97.94	1005.7	97.94
EC1b-116	0.09	8.316	3.059	11.620	0.246	8.139	1426.37	158.8	1422.39	89.14	1418.8	103.67	1426.3	158.80
EC1b-117	0.06	6.139	0.423	9.863	0.045	7.746	865.02	127.3	358.29	29.79	284.86	21.58	284.86	21.58
EC1b-118	0.09	10.59	3.059	14.663	0.245	10.15	1435.83	202.0	1422.48	112.66	1412.8	128.85	1435.8	202.08
EC1b-119	0.10	5.932	3.953	8.490	0.277	6.106	1684.16	109.4	1624.70	68.90	1578.4	85.50	1684.1	109.49
EC1b-120	0.04	10.03	0.099	11.699	0.015	6.055	74.63	238.4	95.99	10.72	96.80	5.82	96.80	5.82
EC1b-121	0.06	10.18	0.829	14.573	0.097	10.44	672.49	217.7	612.94	67.16	596.78	59.54	596.78	59.54
EC1b-122	0.09	5.262	2.770	7.446	0.220	5.307	1450.35	100.1	1347.57	55.61	1283.5	61.77	1450.3	100.16
EC1b-123	0.05	7.017	0.640	9.192	0.081	5.973	509.54	154.2	502.39	36.44	500.76	28.78	500.76	28.78
EC1b-124	0.06	6.172	0.780	8.471	0.092	5.838	667.84	132.1	585.72	37.72	564.72	31.57	564.72	31.57
EC1b-126	0.18	5.497	13.35	7.694	0.521	5.424	2705.94	90.70	2705.28	72.81	2704.6	119.83	2705.9	90.70
EC1b-127	0.05	6.896	0.506	9.472	0.066	6.528	435.91	153.5	415.48	32.31	411.88	26.05	411.88	26.05
EC1b-128	0.06	6.600	0.537	9.244	0.063	6.509	664.67	141.3	436.13	32.79	394.19	24.89	394.19	24.89
EC1b-129	0.05	8.510	0.438	12.140	0.057	8.686	432.51	189.5	369.09	37.59	359.19	30.35	359.19	30.35
EC1b-130	0.08	8.387	1.851	11.622	0.167	8.075	1207.16	165.1	1063.64	76.76	995.46	74.49	511.80	38.05

Table C-2 Rejected Isotopic ratios and Apparent Ages for sample EC1b. Discordance > 20%.

	Isotopic Ratios						Ap. Age							
Sample Name	$^{207}Pb/^{206}U$	1σ abs. err.	$^{207}Pb/^{235}U$	1σ abs. err.	$^{206}Pb/^{238}U$	1σ abs. err.	$^{207}Pb/^{206}U$	1σ abs. err.	$^{207}Pb/^{235}U$	1σ abs. err.	$^{206}Pb/^{238}U$	1σ abs. err.	Best Age	Best Age Error
EC1b-08	0.105	49.356	0.670	80.155	0.046	63.16	1707.23	908.4	520.78	338.57	292.57	180.70	292.57	180.70
EC1b-11	0.089	6.998	0.525	11.539	0.043	9.195	1411.11	133.9	428.36	40.35	268.81	24.21	268.81	24.21
EC1b-16	0.093	7.632	2.269	10.261	0.176	6.885	1492.37	144.4	1202.71	72.44	1047.31	66.56	1047.3	66.56
EC1b-18	0.828	62.696	270.079	94.780	2.365	71.08	4970.20	896.6	5688.59	1803.7	7821.88	3537.4	4970.2	896.69
EC1b-31	0.103	6.767	2.265	12.389	0.159	10.39	1686.60	124.8	1201.55	87.49	949.72	91.79	949.72	91.79
EC1b-41	0.110	11.125	0.792	12.972	0.052	6.698	1791.58	202.6	592.42	58.29	329.35	21.51	329.35	21.51
EC1b-46	0.119	5.794	4.276	7.884	0.261	5.380	1935.39	103.7	1688.67	64.97	1496.17	71.84	1935.3	103.72
EC1b-66	0.022	273.20	-0.165	315.16	-0.056	157.12	0.00	6585.3	0.00	0.00	0.00	0.00	0.00	0.00
EC1b-68	0.112	6.092	3.795	8.883	0.246	6.495	1826.58	110.4	1591.78	71.51	1419.17	82.74	1826.5	110.49
EC1b-75	0.762	57.543	8.921	108.40	0.085	91.87	4851.75	825.9	2329.96	2213.8	524.96	463.98	524.96	463.98
EC1b-85	0.080	7.561	1.684	9.929	0.152	6.466	1206.86	148.9	1002.61	63.34	910.67	54.91	910.67	54.91
EC1b-102	0.073	176.13	0.130	214.71	0.013	122.80	1013.25	3570.2	124.32	256.56	82.81	101.05	82.81	101.05
EC1b-125	0.117	5.746	1.489	10.357	0.092	8.642	1912.47	103.1	925.98	63.00	568.72	47.05	568.72	47.05

Table C-3 Isotopic ratios and Apparent Ages for sample WC2b. Discordance < 20%.

	Isotopic Ratios						Apparent Age							
Sample Name	$^{207}Pb/^{206}U$	1σ abs. err.	$^{207}Pb/^{235}U$	1σ abs. err.	$^{206}Pb/^{238}U$	1σ abs. err.	$^{207}Pb/^{206}U$	1σ abs. err.	$^{207}Pb/^{235}U$	1σ abs. err.	$^{206}Pb/^{238}U$	1σ abs. err.	Best Age	Best Age Error
WC2b-01	0.072	7.942	1.715	11.229	0.174	7.961	974.58	161.95	1014.20	72.14	1031.62	75.89	1031.62	75.89
WC2b-02	0.112	9.664	4.490	13.871	0.290	9.969	1836.15	175.08	1729.12	115.69	1640.46	144.41	1836.15	175.08
WC2b-03	0.074	6.902	1.665	9.367	0.163	6.360	1039.52	139.32	995.17	59.48	974.13	57.51	974.13	57.51
WC2b-04	0.085	6.728	2.432	9.338	0.208	6.503	1307.80	130.60	1251.99	67.29	1218.47	72.21	1307.80	130.60
WC2b-05	0.055	11.170	0.503	16.048	0.067	11.537	394.58	250.49	413.93	54.61	416.92	46.58	416.92	46.58
WC2b-06	0.091	11.359	2.891	16.443	0.230	11.903	1450.26	216.21	1379.52	124.67	1332.76	143.34	1450.26	216.21
WC2b-07	0.090	6.749	3.054	9.453	0.245	6.645	1433.46	128.75	1421.34	72.43	1411.63	84.24	1433.46	128.75
WC2b-08	0.075	10.936	1.763	15.442	0.171	10.918	1059.44	220.10	1032.03	100.38	1017.90	102.81	1017.90	102.81
WC2b-09	0.110	13.434	3.908	21.454	0.256	16.738	1807.53	244.19	1615.26	175.17	1470.11	220.11	1807.53	244.19
WC2b-10	0.069	10.618	0.862	14.046	0.090	9.212	898.36	219.10	630.98	66.10	558.22	49.26	558.22	49.26
WC2b-12	0.085	10.939	2.651	15.315	0.227	10.734	1306.68	212.36	1314.90	113.38	1318.14	127.98	1306.68	212.36
WC2b-13	0.076	7.768	1.777	11.213	0.170	8.107	1089.44	155.65	1037.00	72.98	1010.86	75.85	1010.86	75.85
WC2b-14	0.079	8.051	2.006	11.527	0.185	8.270	1161.19	159.61	1117.56	78.26	1093.70	83.19	1093.70	83.19
WC2b-15	0.063	8.918	0.423	12.599	0.048	8.919	722.08	189.19	357.87	38.02	303.79	26.47	303.79	26.47
WC2b-17	0.076	6.947	1.935	10.025	0.184	7.250	1096.53	139.05	1093.31	67.21	1090.09	72.72	1090.09	72.72
WC2b-18	0.047	22.487	0.098	23.630	0.015	7.281	48.65	537.07	95.07	21.45	96.77	6.99	96.77	6.99
WC2b-19	0.073	9.055	1.731	11.421	0.173	6.984	1000.10	183.90	1020.30	73.64	1028.23	66.37	1028.23	66.37
WC2b-20	0.051	9.227	0.185	12.163	0.026	7.946	261.20	211.89	172.77	19.33	166.12	13.03	166.12	13.03
WC2b-21	0.059	9.516	0.642	12.486	0.079	8.103	568.23	207.12	503.36	49.60	488.47	38.12	488.47	38.12
WC2b-22	0.054	7.313	0.509	10.002	0.069	6.848	356.58	165.10	417.77	34.27	428.29	28.38	428.29	28.38
WC2b-23	0.114	12.740	4.151	17.972	0.264	12.689	1864.14	229.94	1664.47	148.10	1508.75	170.73	1864.14	229.94
WC2b-24	0.079	6.979	2.128	9.746	0.194	6.826	1181.62	137.95	1157.89	67.42	1143.66	71.53	1143.66	71.53
WC2b-25	0.081	10.446	1.276	13.291	0.114	8.237	1217.38	205.40	835.10	75.80	697.80	54.48	697.80	54.48
WC2b-26	0.071	6.700	1.579	9.172	0.161	6.289	964.06	136.84	961.85	57.07	959.56	56.08	959.56	56.08
WC2b-27	0.063	13.563	0.589	18.562	0.068	12.685	715.44	288.07	470.47	70.00	421.21	51.72	421.21	51.72
WC2b-28	0.093	13.234	1.283	19.324	0.099	14.092	1497.79	250.30	838.39	110.72	611.04	82.16	611.04	82.16
WC2b-29	0.077	6.874	1.757	9.434	0.164	6.486	1131.16	136.88	1029.56	61.12	981.12	59.03	981.12	59.03
WC2b-30	0.074	9.247	1.828	12.726	0.178	8.761	1054.71	186.25	1055.47	83.71	1054.49	85.23	1054.49	85.23
WC2b-31	0.074	7.426	1.822	10.099	0.178	6.868	1040.78	149.89	1053.41	66.30	1058.24	67.03	1058.24	67.03
WC2b-32	0.055	8.820	0.524	11.150	0.069	6.844	409.66	197.27	427.84	38.95	430.70	28.51	430.70	28.51
WC2b-33	0.118	37.545	1.519	39.739	0.094	13.037	1920.19	673.25	937.94	248.12	576.45	71.89	576.45	71.89
WC2b-34	0.078	7.809	2.181	11.205	0.202	8.056	1150.16	155.06	1174.98	78.16	1187.25	87.36	1187.25	87.36
WC2b-35	0.083	7.243	2.197	10.150	0.192	7.134	1269.48	141.37	1180.09	70.94	1130.78	73.99	1130.78	73.99
WC2b-36	0.071	10.147	1.599	13.047	0.164	8.221	949.53	207.70	969.64	81.67	977.55	74.57	977.55	74.57
WC2b-37	0.056	10.519	0.453	13.415	0.058	8.345	462.47	233.09	379.04	42.46	365.15	29.62	365.15	29.62
WC2b-39	0.092	6.863	3.132	10.098	0.245	7.429	1476.32	130.17	1440.52	77.87	1415.16	94.41	1476.32	130.17
WC2b-40	0.074	6.866	1.709	9.739	0.168	6.930	1029.57	138.82	1011.75	62.46	1002.67	64.36	1002.67	64.36
WC2b-41	0.058	10.701	0.608	15.000	0.076	10.527	542.92	233.92	482.36	57.66	469.36	47.65	469.36	47.65
WC2b-42	0.089	8.429	2.903	11.689	0.236	8.118	1407.61	161.36	1382.65	88.50	1365.63	99.92	1407.61	161.36
WC2b-43	0.077	10.147	1.851	15.053	0.173	11.133	1132.16	202.01	1063.82	99.55	1030.15	106.01	1030.15	106.01
WC2b-44	0.074	7.192	1.771	9.830	0.174	6.725	1039.60	145.19	1035.05	63.88	1032.26	64.15	1032.26	64.15
WC2b-45	0.099	10.107	4.042	14.609	0.295	10.564	1609.04	188.41	1642.67	119.47	1668.25	155.31	1609.04	188.41
WC2b-46	0.056	28.696	0.138	30.165	0.018	9.318	459.15	636.24	131.12	37.12	113.67	10.50	113.67	10.50
WC2b-47	0.073	8.456	1.746	10.761	0.174	6.680	1001.67	171.71	1025.74	69.58	1036.59	63.97	1036.59	63.97

Table C-3 Continued

WC2b-48	0.057	8.280	0.572	11.587	0.072	8.126	505.80	182.15	459.52	42.85	450.12	35.33	450.12	35.33
WC2b-49	0.050	9.792	0.110	12.355	0.016	7.557	178.65	228.27	105.66	12.40	102.41	7.68	102.41	7.68
WC2b-50	0.109	6.570	4.767	9.326	0.316	6.644	1790.24	119.71	1779.03	78.42	1768.92	102.78	1790.24	119.71
WC2b-52	0.076	7.328	2.026	10.394	0.193	7.396	1098.99	146.61	1124.13	70.77	1136.90	77.09	1136.90	77.09
WC2b-53	0.104	8.241	4.360	11.844	0.304	8.527	1695.55	151.91	1704.76	98.13	1711.89	128.22	1695.55	151.91
WC2b-56	0.058	9.510	0.529	12.961	0.066	8.827	534.88	208.17	431.05	45.55	411.81	35.21	411.81	35.21
WC2b-57	0.099	7.856	3.063	11.117	0.225	7.890	1603.86	146.55	1423.58	85.30	1305.96	93.28	1603.86	146.55
WC2b-58	0.080	7.164	2.246	9.839	0.205	6.772	1188.09	141.47	1195.62	69.24	1199.63	74.13	1199.63	74.13
WC2b-59	0.077	9.796	1.810	12.257	0.171	7.393	1117.31	195.46	1049.22	80.34	1016.70	69.54	1016.70	69.54
WC2b-62	0.074	8.346	1.312	11.060	0.129	7.285	1029.03	168.76	850.89	63.81	784.12	53.79	784.12	53.79
WC2b-63	0.079	7.050	2.149	10.064	0.197	7.210	1174.94	139.48	1164.82	69.85	1159.29	76.50	1159.29	76.50
WC2b-64	0.073	8.334	1.102	11.508	0.109	7.962	1020.26	168.76	754.09	61.32	667.46	50.49	667.46	50.49
WC2b-65	0.078	8.443	2.042	13.134	0.189	10.081	1155.22	167.51	1129.63	89.75	1116.28	103.34	1116.28	103.34
WC2b-66	0.080	8.496	1.784	17.847	0.162	15.709	1195.30	167.60	1039.67	116.64	967.14	141.10	967.14	141.10
WC2b-67	0.054	8.087	0.485	11.259	0.065	7.861	385.35	181.64	401.61	37.36	404.40	30.81	404.40	30.81
WC2b-68	0.077	9.482	1.969	13.372	0.186	9.452	1120.57	189.10	1105.13	90.29	1097.19	95.37	1097.19	95.37
WC2b-70	0.090	9.710	3.055	12.550	0.246	7.980	1424.44	185.46	1421.54	96.30	1419.43	101.67	1424.44	185.46
WC2b-71	0.105	6.824	4.528	9.719	0.313	6.953	1715.09	125.48	1736.10	81.00	1753.31	106.75	1715.09	125.48
WC2b-72	0.072	9.053	1.751	12.675	0.175	8.897	995.96	183.97	1027.48	82.09	1042.15	85.62	1042.15	85.62
WC2b-73	0.076	7.050	1.867	9.781	0.179	6.813	1085.84	141.33	1069.54	64.76	1061.34	66.68	1061.34	66.68
WC2b-74	0.104	7.012	3.639	10.127	0.253	7.339	1701.78	129.16	1558.08	80.83	1453.94	95.53	1701.78	129.16
WC2b-76	0.074	8.359	1.804	11.807	0.177	8.368	1041.08	168.71	1046.88	77.28	1049.35	81.04	1049.35	81.04
WC2b-77	0.082	10.898	2.405	15.456	0.212	10.982	1254.33	213.15	1244.18	111.30	1237.93	123.71	1254.33	213.15
WC2b-79	0.049	21.052	0.174	22.358	0.026	7.563	163.61	492.14	163.03	33.69	162.92	12.17	162.92	12.17
WC2b-80	0.079	8.904	2.014	13.123	0.184	9.665	1175.32	176.16	1120.10	89.26	1091.37	97.04	1091.37	97.04
WC2b-81	0.063	9.085	0.847	11.783	0.097	7.537	716.36	192.92	623.06	54.92	597.32	43.00	597.32	43.00
WC2b-82	0.049	14.783	0.107	19.002	0.016	11.961	164.63	345.53	103.48	18.70	100.77	11.96	100.77	11.96
WC2b-83	0.073	9.278	1.703	13.453	0.169	9.768	1010.85	188.14	1009.76	86.28	1008.57	91.20	1008.57	91.20
WC2b-85	0.048	9.747	0.102	12.665	0.015	8.119	114.65	229.93	98.88	11.93	98.15	7.91	98.15	7.91
WC2b-86	0.076	10.340	1.714	15.070	0.163	10.986	1101.23	206.80	1013.96	96.94	973.24	99.25	973.24	99.25
WC2b-88	0.075	7.302	1.849	9.833	0.178	6.623	1078.18	146.56	1062.99	64.88	1054.64	64.44	1054.64	64.44
WC2b-89	0.056	7.204	0.547	9.646	0.071	6.454	460.08	159.71	442.97	34.64	439.25	27.40	439.25	27.40
WC2b-90	0.074	9.115	1.787	12.906	0.174	9.164	1049.20	183.74	1040.57	84.21	1035.42	87.66	1035.42	87.66
WC2b-91	0.076	7.354	1.703	10.346	0.162	7.311	1103.00	147.04	1009.51	66.27	965.85	65.58	965.85	65.58
WC2b-92	0.072	7.040	1.671	10.049	0.169	7.205	978.86	143.43	997.70	63.92	1005.07	67.05	1005.07	67.05
WC2b-95	0.080	7.347	1.990	9.945	0.181	6.738	1192.27	144.99	1112.20	67.31	1070.27	66.44	1070.27	66.44
WC2b-96	0.054	7.674	0.385	10.349	0.051	6.976	382.50	172.46	330.76	29.22	322.98	21.97	322.98	21.97
WC2b-98	0.049	17.110	0.101	22.302	0.015	14.320	133.98	402.19	97.66	20.77	96.03	13.65	96.03	13.65
WC2b-99	0.060	11.255	0.562	15.280	0.068	10.354	600.81	243.62	453.03	55.90	423.80	42.47	423.80	42.47
WC2b-100	0.046	9.350	0.100	11.412	0.016	6.573	11.60	224.88	97.06	10.56	100.41	6.55	100.41	6.55
WC2b-102	0.063	7.651	0.896	10.458	0.102	7.151	722.22	162.31	649.74	50.23	628.08	42.79	628.08	42.79
WC2b-103	0.058	9.571	0.526	13.591	0.065	9.662	540.40	209.30	429.12	47.60	408.03	38.20	408.03	38.20
WC2b-104	0.063	9.603	0.179	12.092	0.020	7.364	718.31	203.87	167.11	18.63	130.59	9.52	130.59	9.52
WC2b-106	0.053	8.401	0.246	10.985	0.033	7.089	344.73	190.06	223.65	22.05	211.98	14.78	211.98	14.78
WC2b-107	0.075	9.698	1.801	13.220	0.174	8.991	1065.78	195.01	1045.89	86.52	1034.92	85.97	1034.92	85.97
WC2b-108	0.079	8.148	2.015	11.041	0.185	7.458	1172.69	161.25	1120.43	75.06	1092.18	74.93	1092.18	74.93
WC2b-109	0.052	8.621	0.387	11.744	0.054	7.978	297.67	196.66	332.14	33.28	336.60	26.17	336.60	26.17

Table C-3 Continued

WC2b-110	0.072	6.976	1.735	9.701	0.174	6.741	992.19	141.85	1021.73	62.57	1034.26	64.41	1034.26	64.41
WC2b-111	0.085	7.189	2.607	9.814	0.223	6.670	1310.33	139.49	1302.71	72.15	1296.76	78.35	1310.33	139.49
WC2b-112	0.069	12.068	1.086	14.975	0.114	8.855	904.63	248.77	746.38	79.31	694.03	58.26	694.03	58.26
WC2b-113	0.080	11.654	2.136	16.684	0.193	11.929	1205.21	229.55	1160.46	115.89	1135.70	124.23	1135.70	124.23
WC2b-114	0.079	7.598	1.958	10.174	0.181	6.741	1159.99	150.66	1101.36	68.49	1071.17	66.53	1071.17	66.53
WC2b-115	0.058	7.444	0.787	10.055	0.099	6.723	522.27	163.30	589.66	45.00	607.06	38.95	607.06	38.95
WC2b-116	0.081	18.086	0.507	21.836	0.046	12.212	1213.52	355.83	416.27	74.70	287.12	34.29	287.12	34.29
WC2b-117	0.073	16.518	1.788	23.092	0.178	16.117	1014.88	334.75	1041.27	151.50	1053.84	156.72	1053.84	156.72
WC2b-118	0.078	7.997	2.004	10.787	0.186	7.190	1154.66	158.68	1116.97	73.20	1097.85	72.58	1097.85	72.58
WC2b-119	0.051	27.052	0.102	28.369	0.015	8.498	244.10	623.14	98.71	26.69	92.83	7.83	92.83	7.83
WC2b-120	0.096	7.659	3.530	10.527	0.267	7.158	1545.96	143.95	1533.88	83.48	1525.99	97.28	1545.96	143.95

Table C-4 Rejected Isotopic ratios and Apparent Ages for sample WC2b. Discordance > 20%.

	Isotopic Ratios						Apparent Age							
Sample Name	$^{207}Pb/^{206}U$	1σ abs. err.	$^{207}Pb/^{235}U$	1σ abs. err.	$^{206}Pb/^{238}U$	1σ abs. err.	$^{207}Pb/^{206}U$	1σ abs. err.	$^{207}Pb/^{235}U$	1σ abs. err.	$^{206}Pb/^{238}U$	1σ abs. err.	Best Age	Best Age Error
WC2b-11	0.065	35.227	1.912	73.113	0.212	64.070	788.90	739.40	1085.22	531.08	1236.96	724.15	788.90	739.40
WC2b-16	0.102	12.381	2.326	18.323	0.166	13.520	1655.70	229.36	1220.34	130.84	987.86	123.84	987.86	123.84
WC2b-38	0.212	8.196	6.985	10.422	0.239	6.462	2917.23	132.72	2109.56	92.82	1382.92	80.43	2917.23	132.72
WC2b-51	0.171	10.958	2.914	13.235	0.124	7.445	2567.28	183.22	1385.58	100.38	751.09	52.78	751.09	52.78
WC2b-54	0.099	7.106	2.454	9.768	0.180	6.729	1605.19	132.53	1258.61	70.58	1065.64	66.10	1065.64	66.10
WC2b-55	0.075	10.004	1.401	13.517	0.136	9.110	1061.76	201.28	889.18	80.24	821.24	70.25	821.24	70.25
WC2b-60	0.085	11.709	1.938	17.742	0.166	13.344	1309.51	227.23	1094.23	119.37	989.13	122.38	989.13	122.38
WC2b-61	0.082	8.193	0.738	11.641	0.065	8.294	1251.71	160.31	561.50	50.25	406.58	32.68	406.58	32.68
WC2b-69	0.091	8.669	2.036	13.565	0.162	10.454	1451.58	164.98	1127.64	92.62	966.93	93.88	966.93	93.88
WC2b-75	0.088	9.233	2.129	11.753	0.175	7.305	1390.56	177.17	1158.14	81.37	1037.68	70.02	1037.68	70.02
WC2b-78	0.092	7.286	2.032	10.350	0.160	7.385	1467.73	138.35	1126.26	70.55	957.29	65.70	957.29	65.70
WC2b-84	0.129	7.012	4.463	10.571	0.250	7.943	2090.47	123.27	1724.20	87.91	1437.88	102.38	2090.47	123.27
WC2b-87	0.081	7.844	3.355	11.342	0.299	8.224	1226.97	154.02	1494.04	88.95	1687.91	122.15	1226.97	154.02
WC2b-93	0.099	20.172	2.818	29.234	0.206	21.171	1602.61	376.35	1360.28	222.58	1209.90	233.65	1602.61	376.35
WC2b-94	0.081	9.563	1.621	12.068	0.145	7.393	1225.95	187.80	978.50	75.93	870.83	60.23	870.83	60.23
WC2b-97	0.146	17.485	5.378	19.010	0.266	7.489	2302.24	300.38	1881.38	164.18	1522.26	101.55	2302.24	300.38
WC2b-101	0.175	8.918	7.339	12.326	0.304	8.526	2603.52	148.58	2153.55	110.58	1711.65	128.19	2603.52	148.58
WC2b-105	0.091	22.638	1.206	33.812	0.096	25.120	1451.77	430.81	803.54	189.90	589.37	141.50	589.37	141.50